

VibrantLeaves: A principled parametric image generator for training deep restoration models

Raphaël Achddou¹, Yann Gousseau², Saïd Ladjal², Sabine Süsstrunk¹ *Fellow, IEEE*,

Abstract—In this paper, we introduce a synthetic image generator relying on a few simple principles, specifically focusing on *geometric modeling, textures, and a simple modeling of image acquisition*. These principles, integrated into the classical Dead Leaves model, allow for the creation of high-quality training sets for image restoration tasks. Standard image denoising and super-resolution networks trained on these datasets achieve performance comparable to those trained on natural image datasets. The motivation behind this approach stems from the limitations of Deep Neural Networks in image restoration tasks. Despite their impressive performance, these networks are often poorly understood and prone to biases inherited from standard natural image training sets. To mitigate these issues, we emphasize the need for a better control over training sets, particularly through the use of synthetic and abstract datasets. Furthermore, our work includes a detailed analysis of the principles considered, identifying which image properties are necessary for maintaining high performance, thus taking a first step towards explainability. Besides, we show that training neural networks with our synthetic sets improves their generalization capabilities when faced with various perturbations in the test sets.

Index Terms—Image restoration, Synthetic images, Natural Image Statistics.

I. INTRODUCTION

Advancements in image restoration techniques have always been closely tied to the development of image models, due to the inherently ill-posed nature of image restoration problems. Researchers first derived mathematical priors, which were either translated into constrained optimization problems or simple algorithms [1]–[5]. With the advent of deep learning, these classical methods were largely outperformed by deep neural networks (NN). These methods rely on a high volume of data used to iteratively adjust the networks weights for minimizing a loss function, typically the Mean-Square Error [6], [7]. Although these methods have significantly improved the performances on most image restoration tasks, they suffer from several limitations. Neural networks are indeed notoriously bad at generalizing to unseen modalities, be it changes of the image domain or of the type of distortions [8]. Moreover, restoration neural networks tend to hallucinate details that are not present in the original image [9], [10]. Indeed, training image datasets are strongly biased, depending on their content, which may be reflected in restoration results or pose privacy issues. Overall, the complexity of the trained models, due to the large number of network parameters and images in the training sets, makes it challenging to understand their inner workings.

A potential approach to reduce the complexity of this problem is to replace the standard training datasets with synthetic images generated from a small set of parameters. This approach was first proposed in [11] and extended in [12], where training images are synthesized from a *Dead Leaves* (DL) image model. Such images, first introduced to model porous media [13], have then been proposed as a fruitful model for natural images, closely mimicking several of their statistical property [14], [15]. Some of these properties, such as the Laplacian distribution of the image gradient, are assumptions already used in prior-based approaches. By training NNs with such images, the corresponding statistical property are implicitly included in networks *via* the training sets. Even though this approach showed promising results, the performance gap with networks trained on natural images remained significant. As shown in Fig. 1, the image sampled from the classical DL model lack key properties of natural images, such as realistic textures, complex object shapes or depth-related visual cues.

In this paper, we propose a new principled image generator, called **VibrantLeaves**, which incorporates crucial natural images properties: (1) *Geometry*: we generate complex shapes which can recreate arbitrary local curvatures; (2) *Textures*: we propose a simple parametric, exemplar-free, texture generator, which recreates pseudo periodic and random textures; (3) *Depth*: we integrate a depth-of-field simulator along with perspective tilting to reproduce important perceptual depth clues. The code is available on Github for reproducibility.

The corresponding model significantly increases the complexity of the generated images, while still relying on a small set of parameters. These improvements lead to a significant increase in performance of image restoration networks trained on VibrantLeaves images, reaching metrics values almost on par with those of networks trained on natural images with only an average 0.72dB gap in PSNR for image denoising. We further confirm this behavior through super-resolution experiments, as well as deblurring and inpainting experiments in a Plug-and-Play setting [16]. Moreover, the modular framework of VibrantLeaves allows us to understand which properties of natural images are needed to achieve good restoration performance, which is a notable step towards explainable image restoration models. We also show that networks trained on VibrantLeaves images, by inheriting invariance properties of the generating model, generalize better than their natural image counterparts when tested on slightly out-of-distribution datasets.

In short, we can summarize our contribution as follows:

- 1) We propose VibrantLeaves (VL), a principled image

¹ School of Computer and Communication Sciences, EPFL, 1015 Lausanne, Switzerland (e-mail: raphael.achddou@epfl.ch).

² LTCI, Télécom Paris Institut Polytechnique de Paris, 19 Place Marguerite Perey 91200 Palaiseau.

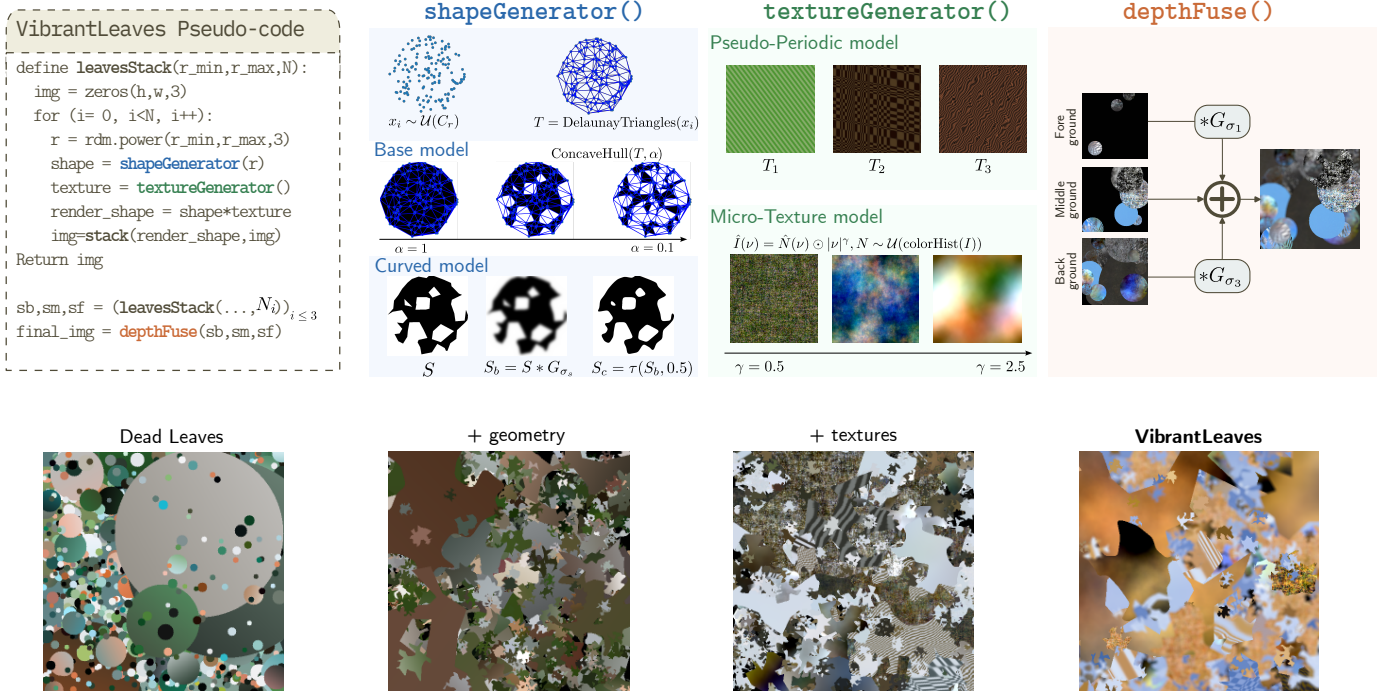


Fig. 1: Graphical summary of the VibrantLeaves model. We integrate three key properties in an occlusion-based model: (1) **Geometry**, through a random shape generator based on concave hulls, (2) **Textures** with an exemplar-free parametric texture generator of both pseudo-periodic and micro textures, (3) **Depth** with a depth-of-field generator and perspective effects. The generated images match natural images statistics much better than other statistical image models, while remaining abstract and free of real image dataset biases.

generator based on the Dead Leaves model, which incorporates essential properties of natural images, such as *geometry, textures, and depth*.

- 2) We show that standard image denoising and super-resolution NNs trained on VL images achieve performance almost on par with NNs trained on natural images. Furthermore, using the PnP setup we can apply our model to any restoration task (in particular inpainting and deblurring).
- 3) As a step toward explainability, we provide a careful analysis of the image properties required to reach good image restoration performance, through ablation studies.
- 4) We show that training with VL images leads to better robustness to various geometric and radiometric perturbations.

II. RELATED WORKS

A. Image restoration: prior-based vs learning based approaches

The goal of image restoration is to retrieve an image as close as possible to the ground-truth image x , starting from altered measurements y . The relationship between x and y can be formulated as follows:

$$y = \Phi(x) + \eta \quad (1)$$

where Φ is a forward operator which often models the acquisition system and η is a random noise, commonly assumed to be an additive white Gaussian noise. Retrieving an estimate \hat{x}

is a notoriously ill-posed problem. In the Bayesian framework, a good estimate is the Maximum-a-Posteriori (MAP) estimator given by:

$$\hat{x}_{MAP} = \arg \max_x p(x|y) \quad (2)$$

$$= \arg \min_x \left[\frac{(\Phi(x) - y)^2}{2\sigma^2} - \log(p(x)) \right] \quad (3)$$

$$= \arg \min_x f(x) + g(x) \quad (4)$$

where σ is the noise standard deviation and $p(x)$ is the unknown prior distribution of natural images. f is called the data fidelity term, and g is called the prior term, which is unfortunately unknown. In order to derive optimization algorithms from this formula, researchers developed a series of analytical priors. These priors impose regularity in the possible solutions, such as smoothness [1], [17] or sparsity [3], [18], [19]. Other standard image restoration methods do not fit this exact framework, but are still based on a regularity principle, such as non-local methods [4], [5], [20], which rely on the hypothesis of self-similarity.

While these methods proved efficient, the focus transitioned to deep-learning algorithms, as they surpassed prior-based approaches on all image-denoising benchmarks [6], [7]. The performance of these models still increases to this day, with the incorporation of more and more complex models such as Transformers [21] or Diffusion models [22]. Deep learning methods aim to learn a direct mapping that minimizes the Mean Square Error (MSE) by optimizing its parameters on a database of clean and noisy image pairs. In this case, the

learnt prior is implicit in the NN parameters, and rather hard to interpret. One can view this implicit prior $\rho_{NN}(x)$ as follows:

$$\rho_{NN}(x) \simeq \mathcal{F}(\text{dataset} \times \text{architecture} \times \text{loss function}, x) \quad (5)$$

where \mathcal{F} is a function which entangles an extremely large number of variables, justifying the often-used “black-box” qualifier given to denoising NNs. Despite this uninterpretable behavior, this implicit prior can be used to solve inverse problems, in Plug-and-Play [16] or stochastic solvers [23].

A recent trend in deep image restoration is to inject more prior knowledge in the design and training of NNs. MWCNN [24] proposes to operate in the wavelet domain to ensure sparsity. Non-local NNs also rely on the hypothesis of self-similarity in the feature space [25], [26]. Finally, additional loss functions can impose constraints on the mapping obtained after training, for instance to better fit with human perception [27], [28]. While these methods focused on the last two variables (architecture and loss function), little effort has been made to better control the properties of the training data for image restoration tasks.

B. Synthetic images for training deep learning models

Using synthetic data for training NNs is a standard procedure used in research fields ranging from medical imaging, to natural language processing, and a wide variety of scientific applications. The reason for this global practice is simple: acquiring real-world data with sufficient diversity can be extremely difficult and costly.

A reasonable criterion for the use of synthetic data is its similarity with real-world data. Note that realism is likely less important for low-level vision tasks, such as optical flow estimation for which the “Flying Chair” and its recent upgrade AutoFlow dataset have proved to be efficient [29], [30]. They both represent flying objects on a fixed background. However, for high-level computer vision tasks such as semantic segmentation [31], instance segmentation [32], object detection [33] and classification [34], photo-realism and meaningful semantic information are very important criteria. Such synthetic image datasets can be extracted from realistic rendering engines [35]–[38], video games [39], or can even be generated with state-of-the-art image generation models [40]–[42]. Training NNs for high-level vision tasks on these datasets can lead to very good performances. However, the methods used to generate these images are either highly engineered (realistic rendering), or highly parametrized (generative models). The main objective of these methods is to generate large volumes of data that resembles the physical world to get perfect annotations such as segmentation masks, bypassing the need for noisy and costly human annotations. Therefore, the implicit prior learned by the NNs on such data is still hard to interpret, and highly biased, either because of the intrinsic bias of the generative models, or through the rendering choices of the user.

In order to tackle this problem, a recent trend in computer vision is to train NNs on abstract images generated with simple random processes, which can in turn generalize well to real-world images. Pursuing this avenue, FractalDB, the seminal work by Kataoka et al. [43], proposes to pretrain

a classification NN on binary images of random fractals, split into different categories, each defined by a mathematical formula and a set of parameters. This work was then extended to the pre-training of Transformer networks [44], or for image segmentation [45]. However Anderson et al. [46] suggest that FractalDB lacks some key properties of natural images to perform competitively with real-world data, such as colors, backgrounds, and occlusions. Achddou et al. [11] proposed to train image restoration networks on synthetic images which exhibit these properties, dead Leaves images, which we will present further. These images match statistics of natural images such as the color histogram, Fourier spectrum, and the distribution of the image gradient [15], [47]. Please refer to Section S8 for a detailed background on the Dead Leaves model. In parallel, Baradad et al. [48] proposed to compare different synthetic abstract datasets for pre-training image classification NNs, reaching good performance with textured dead leaves images, and constrained Style-GAN abstract images. Following these approaches, Madusadhana [49] proposes to include texture by directly sampling a dataset of real-world texture, thus including some bias for the recognition tasks, as NNs are known to be biased toward textures.

III. THE VIBRANTLEAVES MODEL

In this section, we introduce VibrantLeaves, a new synthetic model for training image restoration networks, incorporating simple geometric modeling, textures and depth clues. The proposed algorithm is built upon the Dead Leaves (DL) model, which is extensively described in [50]. An introduction to the model is provided in the supplementary material.

A. Geometry

A limitation of the synthetic dataset proposed in [12] is that dead leaves images are obtained using only disks. While disks are easily generated and guarantee rotation invariance, they are overly simplistic shapes for modeling the variety of shapes of both natural and man-made objects. Common natural structures, such as straight boundaries, corners, holes, or arbitrary local curvatures, cannot occur from superimposing disks.

Therefore, we propose to use a random shape generator, inspired by random polygon algorithms [51], [52] and relying on the notion of concave hull [53] (also called α -shape).

Our generation algorithm consists of the following steps:

- 1) Sample n points $x_i \sim \mathcal{U}(D(0, r))$, with \mathcal{U} the uniform distribution and $D(0, r)$ the disk of radius r ,
- 2) Compute the associated Delaunay triangulation,
- 3) **Concave hull:** For a given $\alpha \in [0, 1]$, remove triangles whose longest edge is larger than $e_{\min} + \alpha \times (e_{\max} - e_{\min})$, without breaking connectivity between all points $(x_i)_{i \leq n}$. Here, e_{\min}, e_{\max} are the smallest and largest edges of the triangulation,
- 4) Rasterize the obtained polygon S
- 5) Apply Gaussian blur $S_b = S * G_{\sigma_s}$ and threshold the resulting image to get $S_c = \tau(S_b, 1/2)$, where τ is the thresholding operator.

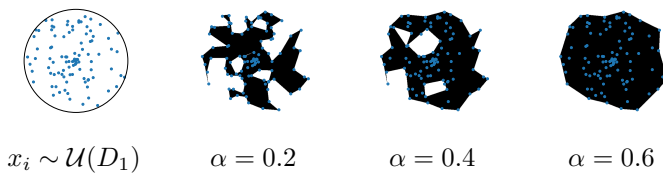


Fig. 2: Random shape generation. We start by sampling n points (here $n = 100$) uniformly in a disk (see first picture), thereafter ensuring rotation invariance. Then, we compute the concave hull of $(x_i)_{i \leq n}$ with a ratio α . As shown here, the larger the α , the closer the concave hull is to the convex hull.

We now clarify our design choices, and some steps of the algorithm. First, we sample points uniformly in a disk to guarantee rotation invariance. Second, we use a concave hull algorithm from the GEOS library [54] which iteratively removes triangles from the Delaunay triangulation according to the procedure above, starting from boundary triangles. This also allows for creating holes, by removing inside triangles.



Fig. 3: Gaussian Smoothing of a random concave hull. From left to right: original shape, shape after Gaussian blurring, and final shape, obtained after thresholding.

Third, in order to get a wide variety of local curvatures, we smooth these random shapes using a rough approximation of the mean curvature motion. We convolve the binary shape mask with a Gaussian kernel G_{σ_s} and threshold the blurred image at level 0.5, as shown in Fig. 3. This smoothing softens the corners, but still maintains the complex structure of the original shape.

The proposed algorithm allows for the presence of concave shapes, acute angles, straight boundaries, holes and a wide variety of curvatures, as can be seen in Fig. 4. It relies only on four parameters: (α, σ_s, n, r) , whose sampling is precised in the supplementary material. The attained complexity and diversity of shapes could not be reached using, e.g., the starred polygons introduced in [51].

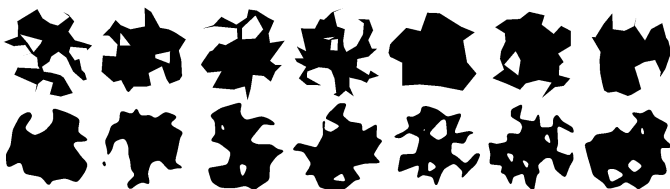


Fig. 4: Samples from our shape generator. First row: sharp polygons. Second row: shapes after Gaussian smoothing.

These shapes are mixed with circles and rectangles in the final VL model. For all shapes, the size distribution is chosen

as a power law $f(r) = C * \mathbf{1}_{[r_{\min}, r_{\max}]}(r) * r^{-\gamma}$, with $\gamma = 3$. This choice of distribution is in agreement with natural image statistics and ensure scale invariance up to the minimal radius r_{\min} . The proportions of each type of shapes and all other hyperparameter choices made in the experimental section will be detailed in the supplementary Section S9.

B. Textures

The synthetic dataset introduced in [12] is obtained from a dead leaves model where each shape is colored uniformly, resulting in flat surfaces. This is a severe limitation to model natural images, where most objects are textured.

Though texture synthesis has been an extensively studied problem, most methods aim at reproducing the visual appearance of an existing exemplar, by either matching its marginal statistics [55], [56], or by smart copy-and-paste [57], [58]. Our purpose is different since we seek a simple yet general enough parametric texture model, for which no exemplar is needed. We focus on two essential aspects of visual textures: repetitions and randomness. We propose two distinct texture generators: a pseudo-periodic pattern generator and a random micro-texture generator, which we combine to create a two-scale texture model.

1) *Pseudo-periodic patterns*: These patterns are common in natural images (zebra fur, honeycombs, etc) and urban scenes (brick walls, windows, etc). To mimic such patterns, we use pseudo-periodic interpolation fields between two randomly sampled colors (c_1, c_2) . Interpolation is performed in CIELAB, as it is a standard color space for which linear interpolation between colors is perceptually meaningful. Colors are sampled in the histogram of a single randomly picked natural image from a natural dataset (in this paper, we will use the Waterloo dataset). This procedure, justified in [11], leads to better color rendering and better restoration performance than a uniform color sampling, which is unnatural, or than a direct sampling from a global dataset histogram, which lacks coherence [59]. Further coherence could be obtained by taking into account second order dependency between colors, but this would imply a much heavier modeling.

We start with simple sine functions $x \mapsto \sin(2\pi x/t)$, where $t \sim \mathcal{U}[T_{\min}, T_{\max}]$. We then apply a sigmoid transform of varying slant to sinusoids, in order to create sharper transitions and enrich the harmonic content of the patterns. We write the resulting field as follows: $S_t(x, y) = \sigma_\lambda(\sin(2\pi x/t))$, where $(x, y) \in \mathbb{R}^2$ is the position and σ_λ is a logit function of growth rate λ , linearly rescaled so that it ranges in $[0, 1]$. In order to obtain random orientations, we rotate this field with an arbitrary angle in $[0, \pi/4]$. To get a 2-dimensional field, we repeat the same process along the y axis, and multiply it with the previously obtained sinusoidal field. The rendered image is the product of the interpolation: $I(x, y) = S_t(x, y) * c_1 + (1 - S_t(x, y)) * c_2$. Examples of such textures are shown in the first column of Fig. 5.

Next, we clip the periodic functions $S_t(x, y)$ with a randomly sampled value $\tau \in [0, 1]$. This allows to create grid-like interpolation fields and thin lines, commonly found in urban and natural environments, as shown in the second column of Fig. 5.

To further enrich our pseudo-periodic patterns, we replace the aforementioned sinusoids with the function $F(x, y)$ described as follows. We start by sampling a sequence of k periods $(t_i)_{i \leq k} \sim \mathcal{U}[T_{\min}, T_{\max}]$. The total length of this sequence is $T = \sum t_i$. We choose to repeat this pattern of k sinusoidal periods, obtaining a global period of T . Writing $\tilde{x} = x \bmod T$, the resulting 1-dimensional oscillatory field writes :

$$F(x, y) = \begin{cases} \sin(\frac{2\pi}{t_0}\tilde{x}), & \text{if } \tilde{x} \in [0, t_0]. \\ \sin(\frac{2\pi}{t_i}\tilde{x}), & \text{if } \tilde{x} \in (\sum_{j=0}^{i-1} t_j, \sum_{j=0}^i t_j]. \end{cases} \quad (6)$$

Same as before, a sigmoid transform σ_λ and a clipping is applied to the obtained field.

Eventually, we randomly distort these interpolation fields by applying random vector fields, obtained from an atmospheric turbulence generator presented in [60]. In short, a random vector field $M \in \mathbb{R}^{(2, H, W)}$ is generated with a white Gaussian noise $M_{i,j} \sim \mathcal{N}(0, 1)$. It is then blurred with a Gaussian kernel of standard deviation s for regularity, and rescaled by a parameter t to control the displacement range. Examples of the obtained texture maps are given in the fourth column of Fig. 5.

2) *Random micro-textures*: Visual textures appear in images at different scales. Pseudo-periodic texture, as presented in the previous section, correspond to the random repetition of textons at a macroscopic scale. However, since the resolution of a sensor is limited, the size of these textons can be much smaller than that of the pixel. This results in a type of texture called micro-textures, very common in natural images, which can be efficiently modeled as Gaussian correlated noises with constrained statistical properties [61]. Grass, sand or clouds taken from afar are examples of such textures.

In terms of statistics, such micro-textures are described by their covariance matrices (and therefore by their power spectrum) and by their color marginals. This property has been used for exemplar-based synthesis of micro-textures by

extracting the texture's power spectrum and randomizing its phase to create new texture maps [61]. Inspired by this method, we propose a parametric random micro-texture generator that does not rely on any exemplar, but on a well know prior: the average profile of the power spectrum of natural images. This power spectrum decays with a $1/|\nu|^\gamma$ rate (where ν is the spatial frequency and γ a parameter) [62], [63].

First, we create a white noise image, by uniformly sampling the color histogram of a randomly picked natural image. As explained before we prefer this approach to a uniform color sampling, as this leads to unrealistic colors, which dramatically affects image restoration performances [11]. Given this noise sample, we impose a linear decay of the power spectrum in the log-domain, with slope γ , resulting in a power spectrum $|\hat{I}(\nu)|^2 \simeq 1/|\nu|^\gamma$. Note that this spectrum model is isotropic as a way to maintain rotation invariance. As shown in Fig. 6, the larger the γ , the smoother the obtained texture.

3) *A micro-macro texture model*: the two previous algorithms focused on either oscillating patterns at a macroscopic scale or micro-textures. However, natural objects can have textures at different scales. For example, a texture of pebbles can be seen as a repetition of similar shape and size, each characterized by a micro-texture. Given the two previous texture models, we propose to merge them into a two-scale texture model. We first start by generating 2 micro-textures maps (T_1, T_2) following the procedure presented in Section III-B2. Then we generate an interpolation mask γ as defined in Section III-B1. We can then blend the two texture maps with this interpolation mask $T_{\text{blended}} = \beta T_1 + (1 - \beta) T_2$. This linear blending is performed in the CIELAB color space. This procedure produces textures at different scales, as illustrated in Fig. 7. The proportions of each type of texture and all other hyperparameter choices made in the experimental section are detailed in the supplementary Section S9.

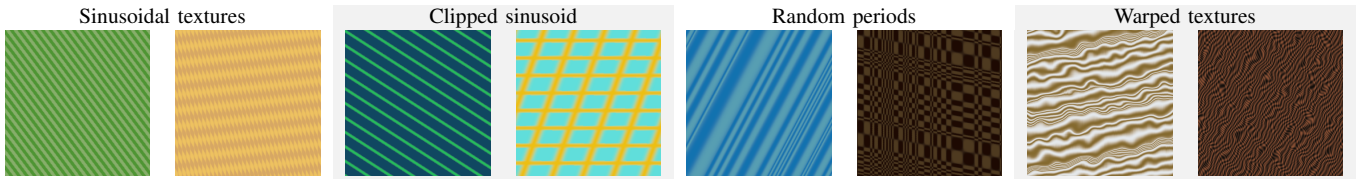


Fig. 5: Pseudo-Periodic textures samples from our texture model in either 1 or 2 dimensions. We start from simple sinusoids and enrich them by: (1) applying a thresholding to the interpolation fields, (2) stacking sinusoids of random periods, and (2) randomly distorting texture maps with gaussian vector fields.

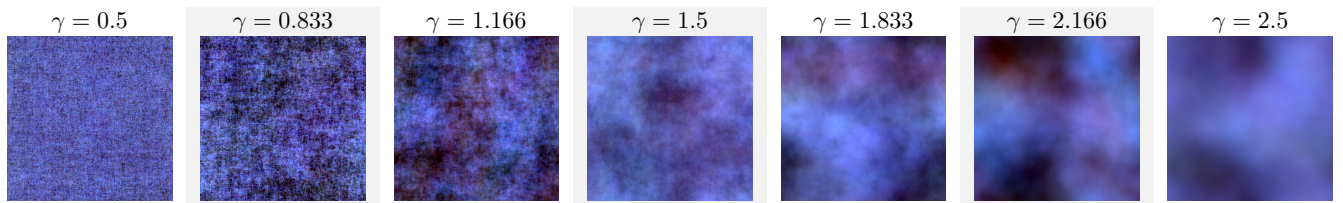


Fig. 6: Samples from our micro-texture model all obtained from the same color histogram. These images are made with colored noise, with an increasing slope γ in the power spectrum from left to right. The smaller the γ , the more present the high frequencies in the image, and the higher the γ , the smoother the texture.

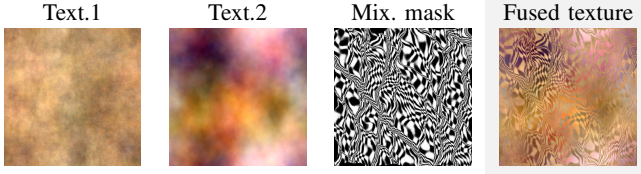


Fig. 7: Macro-Micro texture model.

C. Depth

Physical depth can be perceived in several ways in photographs. Occlusions occur as objects block light-paths from the object to the sensor. Limited depth-of-field causes blur when the aperture of the lens is wide open. Finally, perspective and vanishing points are other depth clues, especially important in urban environments. While the occlusion phenomenon is already properly modeled in classical DL images, perspective and depth-of-field are not. In this section, we propose two additions to better render these properties.

1) *Depth-of field*: In order to recreate this aspect of natural images, a substantial amount of techniques exist in the Computer Graphics literature [64]. For accurate modeling, renderers model the physical response of a lense and use ray tracing. However, this process comes with high computational costs, and requires to model our scene in 3D. Since our goal is to develop simple synthetic models with relatively few parameters, we keep the $2D + t$ approach offered by the dead leaves models and disregard such approaches.

Instead, we use a simpler model, initially proposed for 3D scene rendering, which amounts to split the z-axis in layers and apply different blur kernels for different layers, before combining them in a single fused image [65]. When 3D objects spread over multiple layers, this approach may create artifacts at layers boundaries. Nonetheless, since we consider 2-dimensional shapes that are perfectly parallel to the projection plane, we can use this approach without creating any artifacts.

Consider a foreground image F with support M , in front of a background image B . We assume that the foreground is affected by blur g_F and the background by blur g_B so that the resulting image is approximately given by the formula (which also defines the \oplus operation) :

$$(B, g_B) \oplus (F, g_F, M) := (B * g_B) \times (1 - M * g_B * g_F) + (F * g_F)$$

The main feature of this equation, compared to simple convolutions and masking, is the multiplication part that accounts for the smooth extinction of the background rather than a sharp masking. It should be noted that this formula is exact when the background is in focus ($g_B = \delta$). When the foreground is in focus then the exact version should be

$$B *_v g_B + F (= F * \delta)$$

where the operation $*_v$ is a variable convolution against, not merely g_B , but a variable version of g_B that accounts for the occlusion of the camera lens by the mask M when viewed from the background. Instead of this complex operation we chose to use a smooth extinction that is more tractable.

We consider a stack of three planes I_1, I_2 and I_3 with blurs G_{σ_1}, δ (in focus) and G_{σ_3} respectively and masks M_1 and M_2 (the background I_3 has a trivial mask). Then the final stacking is given by :

$$[(I_3, G_{\sigma_3}) \oplus (I_2, \delta, M_2), \delta] \oplus (I_1, G_{\sigma_1}, M_1)$$

Since the expected benefit of this feature of the model is to obtain realistic transitions (thus involving two objects only) we did not find it useful to consider more than three planes.

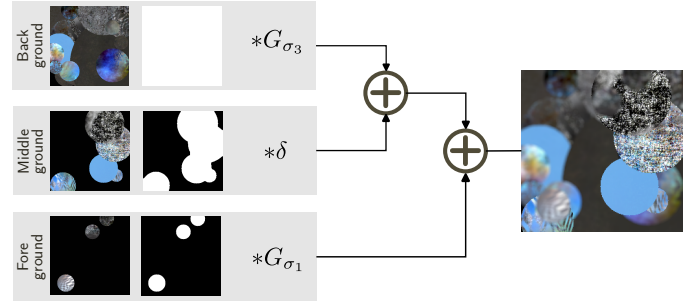


Fig. 8: Depth-of-field diagram

2) *Perspective*: The second property related to depth that we incorporate is perspective. Perspective is particularly visible in images when parallel lines converge to a single point called a *vanishing point*. Instead of operating at the shape level, we directly modify our texture synthesis algorithm to recreate this effect. We apply a perspective homographic transform to texture maps so that the corners coordinates of the original map $p_i \in \mathbb{N}^2, i \in [0, 3]$ are transformed into new corner coordinates \tilde{p}_i . The coefficients of the homography matrix are obtained as the solution of an ordinary least square problem.

IV. EXAMPLES AND STATISTICAL PROPERTIES

Algorithm 1: VL generation algorithm

```

1 function LeavesStack ( $p, w$ )
2   //  $p \in [0, 1]$  corresponds to the expected
   // coverage of the image plane
3   stack, mask  $\leftarrow$  zeros( $w, w, 3$ ), zeros( $w, w$ );
4   while ||mask||/ $w^2 < p \delta$ 
5      $x, y \leftarrow \mathcal{U}[0, w]^2$ 
6     shape_mask  $\leftarrow$  shapeGenerator();
7     texture  $\leftarrow$  textureGenerator();
8     mask  $\leftarrow$  MaskUpdate(shape_mask,  $x, y$ );
9     stack  $\leftarrow$  StackUpdate( $x, y$ , shape_mask,
10      texture);
11  end
12  Output : stack, mask
13 function VL ()
14  // This function merges background,
   // middleground and foreground DL stacks.
15  colors  $\leftarrow$  SampleNatHistogram();
16   $s_b, s_{b, \text{mask}} \leftarrow$  LeavesStack(1/512);
17   $s_m, s_{m, \text{mask}} \leftarrow$  LeavesStack(1/2, 512);
18   $s_f, s_{f, \text{mask}} \leftarrow$  LeavesStack(1/4, 512);
19  merged  $\leftarrow$  depthFuse( $s_b, s_{b, \text{mask}}, s_m, s_{m, \text{mask}}, s_f, s_{f, \text{mask}}$ );
20  output  $\leftarrow$  downScale(merged, 2);
21  Output : output
    
```

Algorithm 1 summarizes the VibrantLeavesformation. More implementations details are provided in the supplementary

Section S9, with a detailed presentation of the hyper-parameters choices. We remind the reader that the code is accessible via the following link. Next, we present some samples of the VL model as well as a statistical evaluation of other synthetic image datasets.

A. Samples of the VL model

The VL model has the ability to render geometry, textures, and depth, and produces images with a much more natural aspect than classical DL. Examples of VL samples are provided in Fig. 9. Additional examples are provided in the supplementary material.

B. Statistical validation

Not only do the generated images seem to perceptually match with natural images better than the standard DL model, they also approach second-order statistics much better. As explained in [14], [15], DL images tend to match two important second-order statistics: the image gradient’s distribution, and the average power spectrum. We will now check that these statistics and others are more faithfully reproduced with the VL model than with the standard DL model. These experiments are mostly provided to illustrate the gain in image faithfulness offered by the proposed model, and not as a measure of success of the proposed approach. Indeed, it would be relatively easy to get better measures by using very large generative models to produce images (which is in contradiction with the goals of this paper), or even by optimizing the parameters of the models.

Regarding the image gradient, we observe in Figure 10 a better match for the VL model. The gradient histogram of DLs images indeed shows a strong peak at zero, which can be explained by piecewise constant surfaces (the leaves). The addition of textures in the VL model mitigates this effect at zero, as seen in the linear plot. Moreover, the profile of the gradient’s histogram of natural images is very close to that of VL images for intermediate gradient values, ie $\|\nabla(I)\| \in [0.1, 0.6]$. Numerically, the Kulblack-Leibler (KL) divergence of the gradient distribution between synthetic and natural images decreases from 0.28 to 0.006 when we go from standard DL images to VL images (see Table I).

Similar conclusions can be drawn for the power spectrum’s profile. In Fig. 10, we report the average power spectrum of different datasets. We represent the spectrum in 1D by averaging the power spectrum radially, assuming rotational invariance. We use a log-log plot to illustrate the $1/|\nu|^\gamma$ behavior of the power spectrum of natural images. We observe in Fig. 10, that the spectrum decay for VL images is similar to that of natural images. We can also estimate γ by running a linear regression in the log-log domain. We obtain $\gamma_{\text{Nat}} = 1.44$, $\gamma_{\text{DL++}} = 1.41$, and $\gamma_{\text{DL}} = 1.79$ (see Table I), which further confirms our observations.

C. Comparison with other synthetic image datasets

In this section, we further analyze the statistical correctness of the proposed VL model by comparing it with other synthetic

datasets, using the three metrics introduced in the previous section. We consider the following datasets:

- **CleVR** [66] made of abstract 3D volumes,
- **FractalDB** [43] made of binary fractal images used for pre-training high-level computer vision models,
- the **textured DL** model presented in [48], also used for pretraining classification models,
- **GTA-V** [39] made of photo-realistic images of a video game in an urban environment,

Same as our model, the first three datasets are made of abstract images, without any semantic information. In contrast, the last one has been carefully designed for photo-realism, and simulates real-world scenes in an urban environment. These synthetic image datasets have been mostly used for training NNs for high level computer vision tasks such as classification and segmentation.

We report naturalness metrics in Table I. In addition to the gradient-KL and the power spectrum slope, we compute the Fréchet Inception Distance (FID) with respect to Waterloo DB, a natural image dataset commonly used for training denoisers. This metric, based on the comparison of deep feature representations extracted with an Inception V3 network trained on Imagenet, is commonly used to assess the quality of generated images and is known to match well with human perception.

As reported in Table I, our model achieves better gradient-KL, and better power spectrum profiles than the other synthetic datasets. While these aspects may be of little relevance for image analysis tasks, they are of prime importance for the training of restoration networks, for which one of the challenges is to restore images while preserving their small scale structure. The FID score is also higher for our model than for others, except for the realistic GTA-5 dataset, which benefit from a higher realism than the VL model and has a slightly better FID score.

In the next section, we report the advantages of the VL model for image restoration tasks.

V. DEEP IMAGE RESTORATION EXPERIMENTS

In [12], classic DL images were used to train image denoising and super-resolution NNs, obtaining promising, but sub-par performance compared to state-of-the-art (SOTA) models trained on natural images. In this section, we will start by showing that the new VL model leads to significant gains in image restoration performance, closing the gap with models trained on natural images for standard restoration NN architectures. Next, we show that networks trained with VL have better robustness to some distortions (rotation and scaling) of the test sets than networks trained on natural images, therefore demonstrating better generalization ability in these settings. Eventually, we assess the importance of each component of the VibrantLeaves model in an ablation study, shedding light on the properties required to train image restoration NNs.

A. Additive White Gaussian Noise Removal

Training Details. We chose to train two different network architectures, a lightweight model FFDNet [6] that is fully

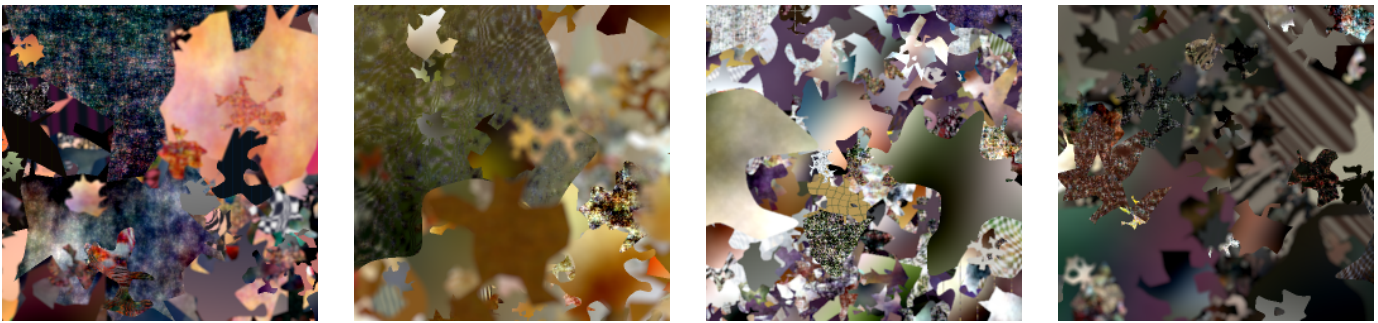


Fig. 9: Examples of samples from the VibrantLeaves model, which integrates modeling for *geometry, textures, and depth*.

convolutional, and a larger model considered as the SOTA in image denoising, DRUNet [7].

For both architectures, we assess the impact of the training data distribution on the denoising performance. Thus, we train multiple versions of the same network on the individual synthetic datasets presented in Table I, ie. FractalDB [43], ClevR [66], GTAV [39], Dead Leaves [11], and DL-textured [48], as well as on natural images. Our natural baselines are trained on a dataset composed of Waterloo DB [67], DIV2K [68] and Flickr database [69], made of roughly 9K images, following the procedure presented in the original DRUNet paper [7].

In order to ensure a similar volume of training data across all our experiments, we synthesize 10K images of size (500×500) with our VibrantLeaves model. Subsequently, we extract 500k patches of size (128×128) from each datasets, as proposed in [70]. We adopted the same training procedures as the ones presented in [6] and [7], by minimizing the \mathcal{L}_2 and \mathcal{L}_1 loss respectively, with an ADAM optimizer and a learning rate decay starting from 10^{-4} and ending at 10^{-6} .

Testing datasets. We tested our models on several classic image denoising benchmarks: Kodak 24 [71], CBSD68 [72], McMaster [73] and Urban100 [74]. The first three testsets mix natural and man-made environments, while the Urban100

dataset only represents urban architectural photographs, exhibiting repetitive patterns at different scales. In order to evaluate the importance of depth-of-field modeling, we also tested our models on the Bokeh validation set [75], made of images with limited depth-of-field.

AWGN removal results. We report the numerical results of our evaluation in Table II, and some examples of visual comparisons in Fig. 11. For both DRUNet and FFDNet architectures, training on VL images improves the results obtained with classic DL synthetic images by a large margin. In terms of PSNR, the gap with networks trained on natural images goes from 2.2dB to 0.72dB in average. Moreover, training on our dataset of VL images leads to better results than training on other synthetic datasets. The margin with abstract procedural models is significant (more than 1.4 dB gap with DL-text). On most testing sets and noise configuration, the model trained on GTA5 images - which represents a realistic urban scenery based on a 3D rendered world-model with semantic information and design biases - performs worse than the model trained on VibrantLeaves images.

Note that the average gap is hindered by the lower performance on Urban100, as this dataset contains perfectly repetitive content which do not match exactly with the semi-periodic texture model we propose, which has random distortions and

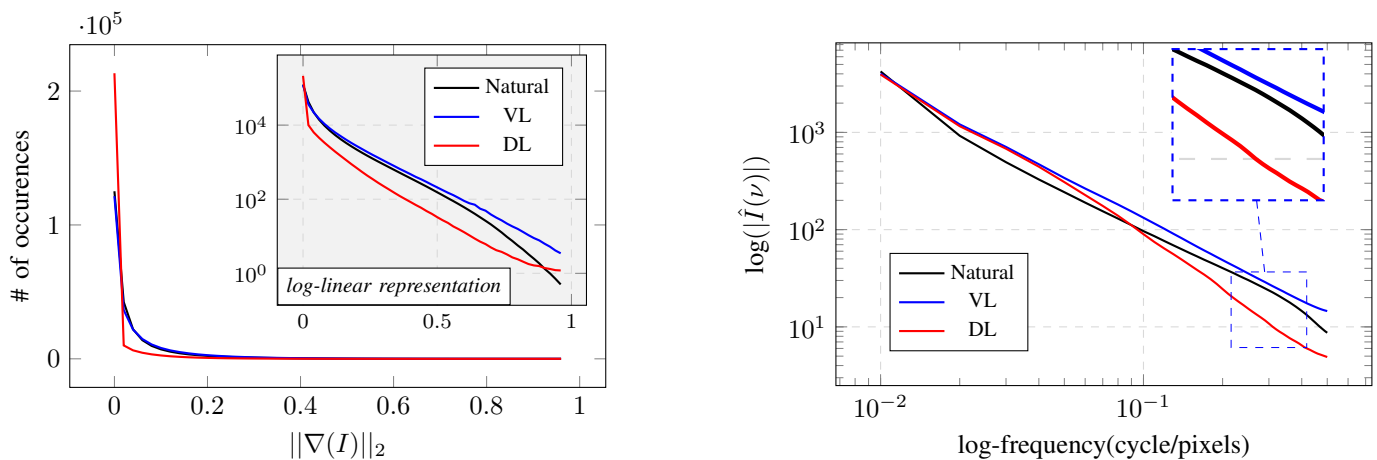


Fig. 10: Comparison of second-order statistics for DL (red), VL (blue) and Natural Images (black). (Left). Histograms of the image gradient $\|\nabla(I)\|_2$ estimated on 1K patches of size (500×500) randomly drawn from each datasets. The grey plot represents the same quantities in a log-linear representation for better visualization of the behavior at higher gradient values. (Right). Average 1D power spectrum $(|\hat{I}(\nu)|)$ in a log-log representation for each datasets.

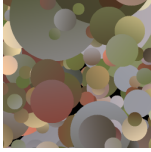
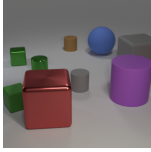
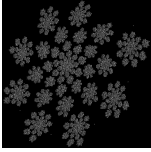
Dataset	DL [11]	ClevR [66]	GTA-5 [39]	FractalDB [43]	DL-textured [48]	VL
Samples						
$KL\text{-Gradient} \downarrow$	0.286	0.517	<u>0.015</u>	1.917	0.228	0.006
$\gamma_{\text{Spectrum}} (\gamma_{\text{Nat}} = 1.43)$ (R^2)	1.73 (0.992)	1.67 (0.992)	<u>1.49</u> (0.982)	0.51 (0.584)	0.99 (0.98)	1.41 (0.995)
$FID \downarrow$	318	217	186	342	312	<u>193</u>

TABLE I: Comparison of image “naturalness” metrics for different synthetic datasets. We report the FID, the KL of the gradient’s distribution computed with respect to the natural images from WaterlooDB, and the slope γ of the average power spectrum (with its linear regression score R^2). Overall, VL has better metrics than other synthetic image datasets.

Method / σ	Kodak24		CBSD68		McMaster		Urban100		Bokeh		Average	
	25	50	25	50	25	50	25	50	25	50	25	50
Input PSNR	20.43	14.86	20.53	15.01	20.91	15.38	20.63	15.11	20.46	14.95	20.59	15.06
DRUNet _{Fractal} [43]	17.32	17.06	17.05	16.66	15.57	15.19	16.20	15.93	19.49	18.47	17.13	16.66
DRUNet _{ClevR} [66]	30.42	27.71	29.45	26.64	30.98	28.15	29.43	26.05	37.13	33.91	31.48	28.49
DRUNet _{DL} [11]	30.95	28.09	30.20	27.18	31.25	28.32	29.43	26.05	36.66	33.76	31.69	28.68
DRUNet _{DL-Text} [48]	31.14	28.11	30.35	27.18	31.33	28.31	29.26	25.81	37.19	33.90	31.85	28.66
DRUNet _{GTA5} [39]	32.14 [†]	<u>29.20[†]</u>	31.14 [†]	<u>28.06[†]</u>	32.43 [†]	29.47 [†]	31.17 [†]	27.90 [†]	38.59 [†]	35.71 [†]	33.09 [†]	30.07 [†]
DRUNet _{VL}	<u>32.16</u>	29.16	31.21	<u>28.06</u>	<u>32.63</u>	<u>29.59</u>	31.27	27.94	<u>38.70</u>	35.78	<u>33.19</u>	30.11
DRUNet _{Nat}	32.89	29.86	31.69	28.51	33.14	30.08	32.60	29.60	39.21	36.31	33.91	30.86
FFDNet _{Fractal} [43]	18.08	17.08	17.98	17.01	16.82	15.94	17.44	16.50	19.11	18.08	17.82	16.92
FFDNet _{ClevR} [66]	30.14	27.50	29.31	26.58	30.05	27.47	27.90	25.09	36.24	33.40	30.73	28.01
FFDNet _{DL} [11]	30.91	28.02	30.23	27.19	31.10	28.18	29.21	25.79	36.36	33.45	31.56	28.52
FFDNet _{DL-Text} [48]	31.14	28.11	30.35	27.19	31.33	28.32	29.26	25.81	37.19	33.90	31.85	28.52
FFDNet _{GTA5} [39]	31.46	28.52	30.56	27.55	31.30	28.47	29.68	26.48	37.39	34.29	32.08	29.06
FFDNet _{VL} [11]	31.72	28.61	30.85	27.68	31.85	28.78	30.18	26.73	37.85	34.43	32.49	29.24
FFDNet _{Nat}	32.13	28.98	<u>31.21</u>	27.96	32.35	29.18	<u>31.40</u>	<u>28.05</u>	38.28	35.05	33.07	29.84

TABLE II: Image denoising results. We report the PSNR of two denoising networks (DRUNet [7] and FFDNet [6]) trained on either natural images or synthetic images (Dead Leaves or VibrantLeaves). The models are tested on several image denoising benchmarks. Best results are in **bold** and second results are underlined.

oscillations.

This global improvement in PSNR also correlates well with the visual quality of the denoised results shown in Fig. 11. The examples show much better restoration of semi-periodic (see the first example) and micro-textures (see the second example). The model trained on DL sometimes tends to combine small circles in order to recreate complex structures from the original image. A more in-depth analysis of the benefits of the VL model for image denoising is presented in Section VI-B, where each addition of the model is analyzed.

Interestingly we observe that, when training with the DL model, switching FFDNet for DRUNet for the standard DL model leads to marginal improvements. In contrast, the improvements provided by the change in architecture are greater for other training sets, including the VL one. This suggests that performances are somehow upper-bounded when training with the DL model, which we may interpret as a lack of expressiveness of this image model. On the contrary, we do not observe this behavior with the VL model, suggesting that it is expressive enough for SOTA image restoration NNs.

B. Single-Image Super-resolution (SISR)

Training Details. We chose the Swin-IR lightweight model [76] for SISR at both scale 2 and 4. We trained these networks with images from either the Dead Leaves model [11] and the VibrantLeaves model. More precisely, we generated 10K patches of size (256×256) and downsampled them using the Matlab’s bicubic downsampler (which is standardly used in SISR benchmarks) with scales 2 and 4. We trained these networks following the optimization schedule and code provided by the authors of [76].

Testing datasets. We tested our models on several classic SISR benchmarks: Set5 [71], Set14 [77] and DIV2K [68] validation sets. Note that DIV2K’s training set was used for the training of SwinIR original model.

SISR results. We report numerical results in Table III and visual results in Fig. 12. In terms of PSNR, the gap between Swin-IR_{VL} and Swin-IR_{Nat} is in average of 0.76dB for scale $\times 2$ and 0.51dB for scale $\times 4$, while it was 2.1dB and 1.39dB for Swin-IR_{DL}.

Note that the gap is larger on the DIV2K testset which is very similar to the training set of Swin-IR_{Nat}. These perfor-

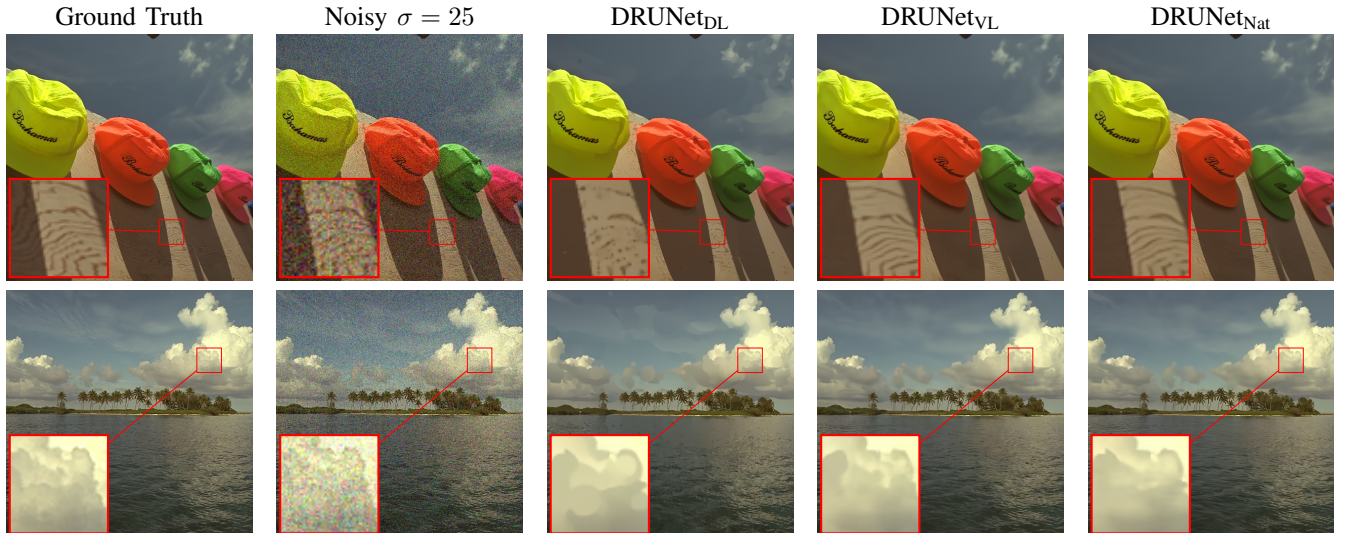


Fig. 11: Visual results for AWGN denoising (best viewed on a digital screen). We compare the same DRUNet architecture trained either on Dead Leaves [11], VibrantLeaves, or natural images.

Scale	Method	Set5 [71]	Set14 [77]	DIV2K [68]	Average
x2	Swin-IR _{Nat}	38.14	33.86	36.46	36.15
	Swin-IR _{VL}	<u>37.39</u>	<u>33.29</u>	<u>35.48</u>	<u>35.39</u>
	Swin-IR _{DL}	35.92	32.03	34.19	<u>34.04</u>
x4	Swin-IR _{Nat}	32.44	28.77	30.65	30.62
	Swin-IR _{VL}	<u>31.76</u>	<u>28.49</u>	<u>30.08</u>	<u>30.11</u>
	Swin-IR _{DL}	30.60	27.76	29.31	<u>29.22</u>

TABLE III: Results for Single-Image Super-Resolution. The models are tested on several SISR benchmarks. Best results are in **bold** and second results are underlined.

mance gains translate to better image quality, as illustrated in Fig. 12. Both examples show that Swin-IR_{VL} corrects two major defects of Swin-IR_{DL}: the incapacity to properly restore lines (second example), and the creation of staircasing artifacts (first example). The results of Swin-IR_{VL} appears almost as sharp as those of Swin-IR_{Nat}.

C. Plug-and-Play for Inverse Problems

Background on Plug-and-Play (PnP) methods Many image restoration problems can be formulated with the linear inverse problem setup presented in Eq. (1), for which $\Phi(x) = Ax$ where A is assumed to be known, or measurable. Optimization-based algorithms for inverse problems can be derived from the MAP estimator formulation Eq. (4), by replacing the term $g(x)$ with a regularity hypothesis [2], [3]. Among these optimization algorithms, variable splitting descent methods such as HQS or ADMM have emerged as practical solvers. The problem can be rewritten as $\arg \min f(x) + g(z)$ s.t. $z = x$, such that the algorithms alternate between a descent step on f and a descent step on g . For such algorithms, Venkatakrisnan et al. [16] first showed that the descent step on the prior g is equivalent to a denoising. Thus, any denoising algorithm, and in particular deep denoisers [7] can be used to replace this descent step, while the other step can be computed

in a closed form (at least for Gaussian noise). This elegant trick allows any pre-trained denoiser to be used for solving a wide variety of image restoration tasks without any retraining, while attaining impressive restoration results. This is due to the fact that deep denoisers encapsulate regularity models that are more refined than a simple function $g(x)$. Therefore, we can assess the power of our VL image generator by training a denoiser on VL images and use the resulting denoiser in a in PnP setup.

In the following experiments, we will compare PnP results using either our DRUNet_{VL} denoiser or DRUNet_{Nat}, for both image deblurring, and image inpainting experiments. We will use the DPIR algorithm [7], which is based on HQS and an ad-hoc noise scheduler, as our PnP setup.

Image Deblurring. The associated inverse problem writes as follows:

$$y = k * x + n, \quad (7)$$

where k is a motion blur kernel from the set of Levin et al [78], and $n \sim \mathcal{N}(0, \sigma^2)$ for which we set $\sigma = 7/255$. We test three of the proposed kernels on the standard Set14 dataset. We report PSNR results for deblurring in the first 3 columns of Table IV. Numerically, the gap between DPIR_{VL} and DPIR_{Nat} is in the range [0.38, 0.5] dB while the gap with DPIR_{DL} is in the range [2.23, 2.4]dB. Visually the results are also much improved, as DPIR_{DL} leads to the creation of disk-like homogeneous shapes, while our DPIR_{VL} correctly restores textures and object boundaries.

Image Inpainting. In this case the linear degradation operator consists in multiplying $p\%$ of the pixels by 0 leaving the other unchanged. The problem is then to retrieve the hidden pixels (we do not consider additional additive noise). Again, in table IV we can see the results of using VL instead of natural images for training in a PnP setup. We also achieve a gap of [0.32, 0.5] w.r.t. to natural training.

TABLE IV: Plug-and-Play numerical results. Tests are performed on the dataset Set14 [77], with a Gaussian noise of std $\sigma = 7$ for deblurring. Best results are in **bold**, second are underlined.

Problem Prior / level	Deblurring			Inpainting	
	k_0	k_1	k_2	$p = 50\%$	$p = 70\%$
DPIR _{DL}	27.43	27.15	27.46	29.29	26.41
DPIR _{VL}	<u>29.33</u>	<u>29.07</u>	<u>29.31</u>	<u>30.29</u>	<u>27.08</u>
DPIR _{Nat}	29.83	29.54	29.69	30.78	27.40

VI. INVARIANCES AND ABLATION STUDIES

A. Invariance analysis of the trained models

In the previous section, we have shown that natural images can be replaced by the proposed VL synthetic images for training restoration NNs, with limited performance loss. In this section, we show that such training also yields better generalization ability of the resulting networks. Indeed, many studies showed that neural networks are often over-specialized to the training distribution [8], [79], leading to poor generalization capability to out-of-distribution samples. In the case of images, such samples can be obtained by distorting the original test data with simple operations such as contrast manipulations, rotations or downscaling. In order to deal with these issues, one could either augment training data with these distortions or develop neural architecture which are invariant to these specific distortions [80]. However these solutions fall short when the model is confronted to unseen distortions.

Conversely, the VL model is intrinsically invariant to many transformations, and in particular to scaling and rotation. In the following experiments, we show that these property yield better generalization abilities by testing NNs trained on VL or natural images on distorted images.

1) *Protocol:* We compare DRUNet_{Nat} and DRUNet_{VL} on slightly modified versions of the images of the Kodak24 dataset to which we add noise at standard deviation $\sigma = 25$.

For each type of distortion, we test our denoising NNs on various distortion levels. In order to assess how the distortion affects the denoising performance, we measure the PSNR difference induced by each distortion level β for both denoising NNs. For each denoiser f , this difference amounts to

$$\Delta_f(g, \beta) = \text{PSNR}(f(g(X, \beta), 25)) - \text{PSNR}(f(X, 25)),$$

where $g(\cdot, \beta)$ is the distortion function, and X are the Kodak images. When comparing two denoisers (f_1, f_2), $\Delta_{f_1} > \Delta_{f_2}$ means that model f_1 is more robust to the tested distortion than model f_2 . That is why we also report the evolution of:

$$\Delta(g, \beta) = \Delta_{\text{DRUNet}_{\text{Nat}}}(g, \beta) - \Delta_{\text{DRUNet}_{\text{VL}}}(g, \beta)$$

with respect to β .

The distortions we consider are the following:

- *Rotation:* $g_{\text{rot}}(I, \theta)$, implemented using a linear interpolation, which results in a small loss of high frequency,
- *Scale:* $g_{\text{scale}}(I, \gamma) = \text{Bicubic} \downarrow_{\gamma} [G_{\sigma(\gamma)} * I]$, where $\sigma(\gamma)$ is a linear function that sets the standard deviation of the gaussian kernel depending on the downscaling factor, to ensure no aliasing.

2) *Results:* In Fig. 14, we report $\Delta_f(g, \beta)$ for both distortions in separate plots. In each plot, we report $\Delta_{\text{DRUNet}_{\text{Nat}}}(g, \beta)$ in black and $\Delta_{\text{DRUNet}_{\text{VL}}}(g, \beta)$ in red. We also report Δ for each distortion.

For both distortions, we observe that the red curve is always above the black curve, meaning that our version of DRUNet trained on VL is more robust to these distortions.

Interestingly, $\Delta(g_{\text{scale}}, \gamma)$ increases with the distortion level. On the other hand, $\Delta(g_{\text{rot}}, \theta)$, has a symmetric profile, and reaches a maximum for $\theta = 45^\circ$. This is because DRUNet_{Nat} was trained with images rotated with $\theta \in \{90, 180, 270\}$. Therefore, $g_{\text{rot}}(\cdot, 45)$ is the rotation that maximizes the distance with the training distribution.

Overall, these experiments suggest that training with VL images improves the robustness of our model to simple distortions. Incorporating invariances in the data itself appears

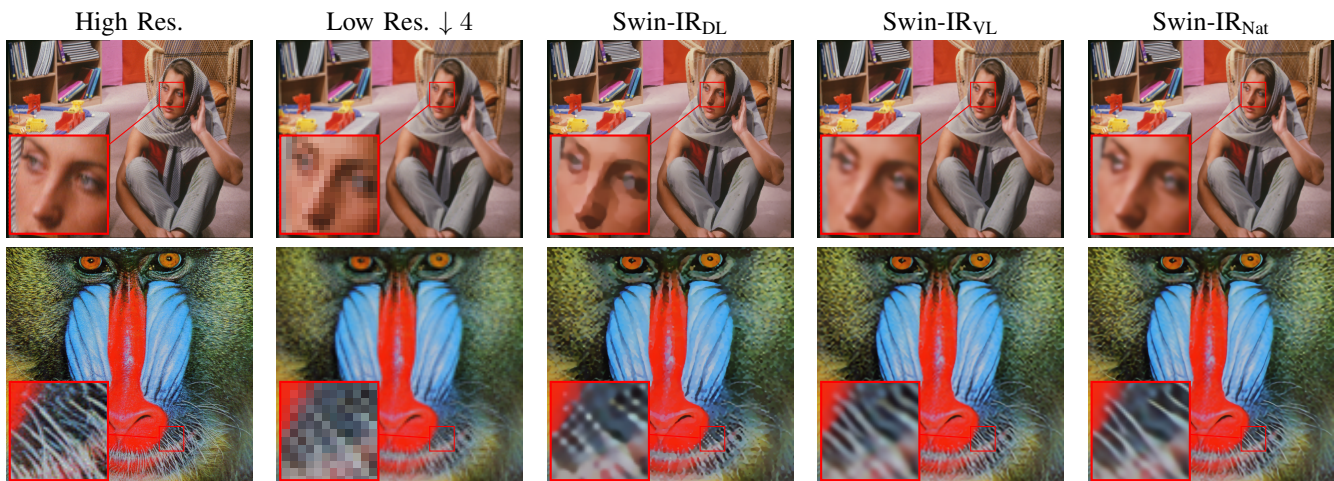


Fig. 12: Visual results for Single-Image-Super-Resolution (best viewed on a digital screen). We compare the same SwinIR architecture trained either on Dead Leaves [11], VibrantLeaves, or natural images. The results suggests that Swin-IR(DL) creates staircasing artifacts (first line) and can't recreate linear objects and textures(second line).

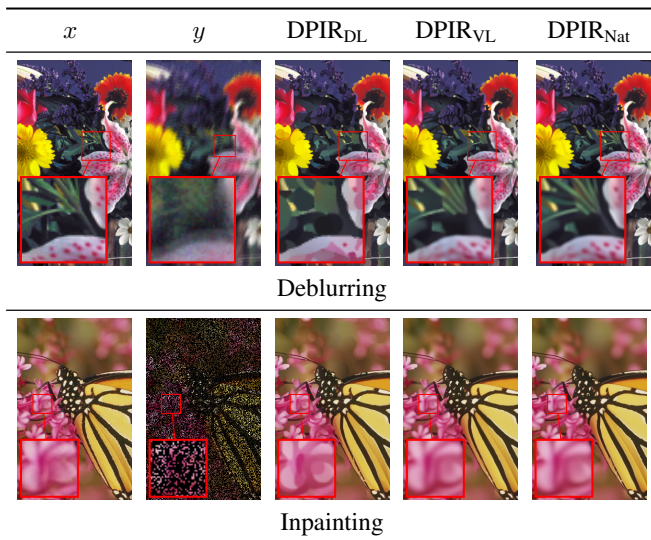


Fig. 13: Plug-and-Play Deblurring and Inpainting. We compare three different priors in the DPiR framework: DRUNet_{DL}, DRUNet_{VL} and DRUNet_{Nat}. Perceptually, results from DRUNet_{VL} and DRUNet_{Nat} are very similar. Best viewed zoomed in.

to be a simpler way to incorporate invariances in the learned model than to modify the architecture of the network. The VL model is a simple candidate to integrate such invariances, while maintaining high restoration performance.

B. Ablation Study

In order to assess the respective importance of each property incorporated in VibrantLeaves, we perform an ablation study on the generation algorithm. We generate 10K (512 × 512) images, removing one or more properties of the proposed VibrantLeavesmodel. We consider the following settings:

- **VibrantLeaves**: all properties combined.
- **Without Depth**: we remove depth-of-field modeling and perspective.
- **Without complex shapes**: images are generated with disks only.
- **Without micro-textures**: the textures are sampled from the semi-periodic texture generator only.
- **Without periodic textures**: the textures are sampled from our micro-texture generator only.
- **Without textures**: the shapes are generated with constant colors.
- **Without depth and textures**: the random shapes are generated without textures and without depth-of-field simulation.
- **Dead Leaves**: the original model from [12].

For each of these settings, we train a DRUNet denoising network with the same optimization framework. We test the obtained models on three datasets: Kodak24, the Bokeh dB and Urban100. We report numerical evaluations in Fig. 15 and visual comparisons in the Supplementary Fig. S1.

Depth. While removing depth-of-field and perspective doesn't impair performance too much on Kodak24, there is a significant gap for the Bokeh dataset, which contains images

with limited depth-of-field. Visually, the denoised images have strong artifacts in blurry areas: the model tends to hallucinate sharp boundaries, as can be seen in the first row of Fig. S1. One can also compare models ● and ●, which do not have texture modeling. In this case, removing depth-of-field simulation leads to a gap of more than 1dB between these two models for the Bokeh dataset. Additionally, the gap in performance for Urban100 between models ● and ○ is a bit larger than for Kodak24, as this dataset mostly contains images with perspective.

Textures. Texture plays a major role in the success of our proposed model. Looking at the results of ablated model ●, we see that semi-periodic textures are necessary for modeling urban environments, which include repetitive patterns. Visually, model ● cannot recreate such patterns, as we can see in the second row of Fig. S1. Regarding micro-textures, the numerical results of model ● suggest that this aspect of the proposed model is of limited importance for quantitative performance. However, removing such patterns leads to obvious artifacts in micro-textures as we can see in the third row of Fig. S1, where grass patterns are recreated with distorted sinusoidal patterns. Finally, removing both types of textures leads to a significant performance drop (model ●). These observations suggests that both texture models complement each other.

Shapes. Texture and depth modeling seem to be the most important aspects of our model. Also, the performance gap between model ● and ○ is relatively small, which could indicate that shape modeling is not crucial. However, if we compare models ● and ●, which do not have any texture or depth modeling, the addition of complex shapes in ● leads to significant performance improvements in PSNR, as reported in Fig. 15. In addition, we observe a larger PSNR gap between ● and ○ for the Urban100 dataset, which mostly contains straight boundaries between objects and right-angled corner which can not be obtained with model ●, as it is based on disks.

VII. CONCLUSION AND PERSPECTIVES

In a previous work, [11], we had shown that Dead Leaves images were a promising replacement of natural images for the training of image restoration NNs, despite a significant performance gap. In this paper, we introduce VibrantLeaves(VL), a principled parametric image model based on the Dead Leaves framework which further incorporates three key image properties: complex geometry, texture modeling and physical depth. We show that the VL model yields near SOTA performance on two restoration tasks, reaching on average a 0.72 dB PSNR difference for image denoising, and 0.5 dB for single image super-resolution. We also study the respective importance of each component of the model in a detailed ablation study, each one being important for restoration performance. We believe that such experiments are a direct way to understand what a good prior for natural images is, providing some understanding on deep restoration methods. Last, we provide simple experiments suggesting that synthetic training can improve generalization, leveraging invariance properties of the training set. Further demonstrating and exploiting such generalization ability would be a natural follow-up of this work.

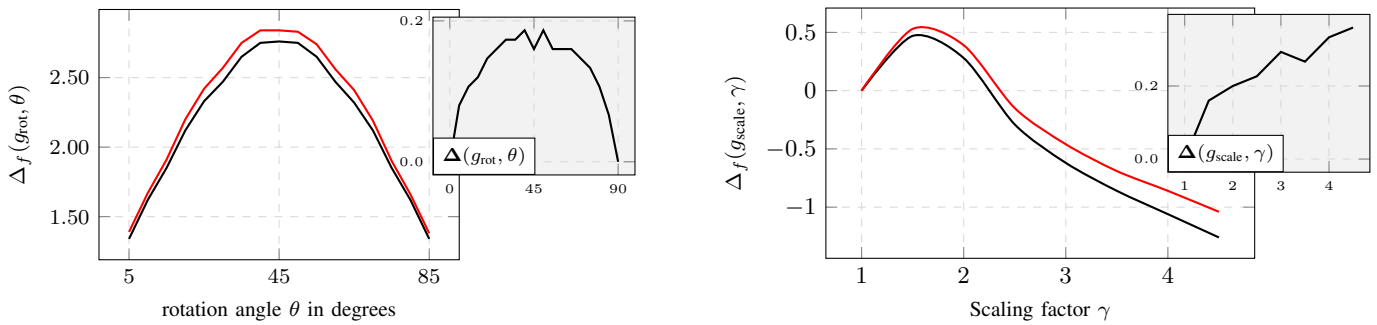


Fig. 14: Invariance experiments. These plots show the PSNR difference between DRUNet_{Nat}(in black) and DRUNet_{VL}(in red) tested at $\sigma = 25$ on slight modifications of the Kodak24 dataset: rotations with an angle $\theta \in [5, 85]$ degrees, and downscaling with an increasing factor $\gamma \in [1, 4.5]$.

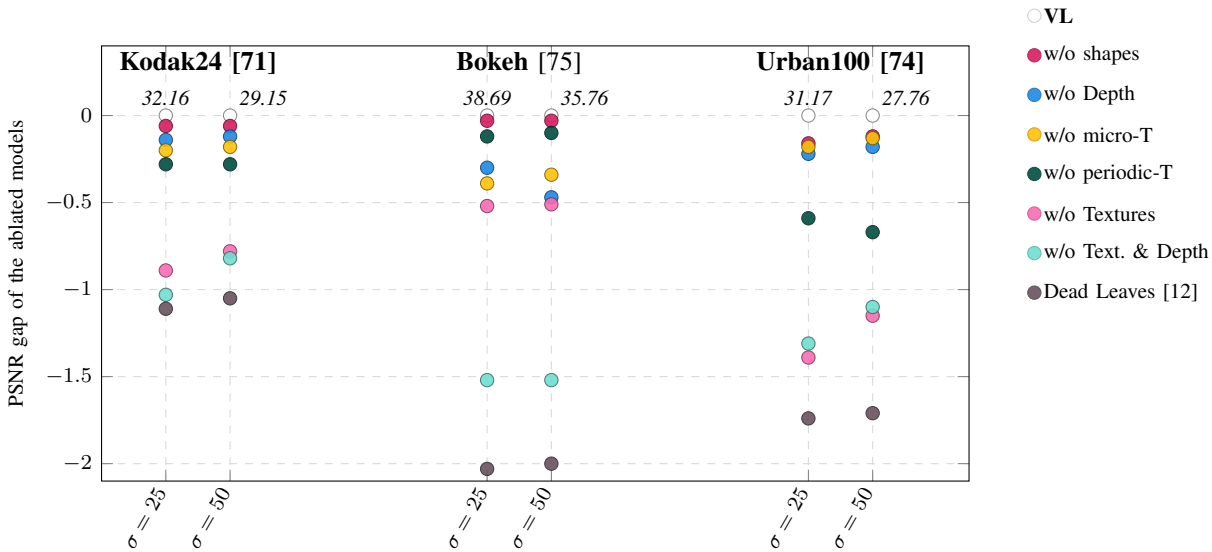


Fig. 15: Ablation study - Numerical results. We report the PSNR gap of the ablated models with respect to the results of DRUNet trained on VibrantLeaves. We test each models on two different noise values ($\sigma \in \{25, 50\}$) and different natural image datasets with different properties: Kodak24 [71], BokehDB [75], Urban100 [74]. The score on top of each column refers to the PSNR of DRUNet trained on VibrantLeaves.

Another asset of the proposed approach is that it provides direct control of the biases of the trained model. Indeed, models trained using massive and often not well-controlled natural image datasets are prone to hallucinations, which is particularly problematic in satellite or biomedical imaging. An interesting perspective would be to explicitly show the biases of the learned implicit prior by sampling from it [23]. We also believe that the proposed approach can yield other clues toward deep architectures understanding. As our model has few parameters, a potential way to add more interpretability would be to back-propagate through these parameters to find out which settings of the VL model most likely led to the restored image by adapting attribution methods.

REFERENCES

[1] N. Wiener, *Extrapolation, interpolation, and smoothing of stationary time series: with engineering applications*. The MIT press, 1949.

[2] D. Donoho and I. M. Johnstone, “Ideal Spatial Adaptation by Wavelet Shrinkage,” vol. 81, no. 3, pp. 425–455, 1994.

[3] L. I. Rudin, S. Osher, and E. Fatemi, “Nonlinear total variation based noise removal algorithms,” *Physica D: nonlinear phenomena*, vol. 60, no. 1-4, pp. 259–268, 1992.

[4] A. Buades, B. Coll, and J.-M. Morel, “A non-local algorithm for image denoising,” in *2005 IEEE Computer Society Conference on Computer Vision and Pattern Recognition (CVPR’05)*, vol. 2. IEEE, 2005, pp. 60–65.

[5] K. Dabov, A. Foi, and K. Egiazarian, “Video denoising by sparse 3D transform-domain collaborative filtering,” *European Signal Processing Conference*, vol. 16, no. 8, pp. 145–149, 2007.

[6] K. Zhang, W. Zuo, and L. Zhang, “Ffdnet: Toward a fast and flexible solution for cnn-based image denoising,” *IEEE Transactions on Image Processing*, vol. 27, no. 9, pp. 4608–4622, 2018.

[7] K. Zhang, Y. Li, W. Zuo, L. Zhang, L. Van Gool, and R. Timofte, “Plug-and-play image restoration with deep denoiser prior,” *IEEE Transactions on Pattern Analysis and Machine Intelligence*, 2021.

[8] T. Plotz and S. Roth, “Benchmarking denoising algorithms with real photographs,” in *Proceedings of the IEEE conference on computer vision and pattern recognition*, 2017, pp. 1586–1595.

[9] A. Goujon, S. Neumayer, and M. Unser, “Learning weakly convex regularizers for convergent image-reconstruction algorithms,” *SIAM Journal on Imaging Sciences*, vol. 17, no. 1, pp. 91–115, 2024.

[10] M. El Helou and S. Süsstrunk, “Bigprior: toward decoupling learned prior hallucination and data fidelity in image restoration,” *IEEE Transactions on Image Processing*, vol. 31, pp. 1628–1640, 2022.

- [11] R. Achddou, Y. Gousseau, and S. Ladjal, "Synthetic images as a regularity prior for image restoration neural networks," in *International Conference on Scale Space and Variational Methods in Computer Vision*. Springer, 2021, pp. 333–345.
- [12] —, "Fully synthetic training for image restoration tasks," *Computer Vision and Image Understanding*, vol. 233, p. 103723, 2023.
- [13] G. Matheron, "Modele séquentiel de partition aléatoire," Technical report, CMM, Tech. Rep., 1968.
- [14] L. Alvarez, Y. Gousseau, and J.-M. Morel, "The size of objects in natural and artificial images," in *Advances in Imaging and Electron Physics*. Elsevier, 1999, vol. 111, pp. 167–242.
- [15] A. B. Lee, D. Mumford, and J. Huang, "Occlusion models for natural images: A statistical study of a scale-invariant dead leaves model," *International Journal of Computer Vision*, vol. 41, no. 1-2, pp. 35–59, 2001.
- [16] S. V. Venkatakrishnan, C. A. Bouman, and B. Wohlberg, "Plug-and-play priors for model based reconstruction," in *2013 IEEE global conference on signal and information processing*. IEEE, 2013, pp. 945–948.
- [17] C. Chu, I. Glad, F. Godtlielsen, and J. Marron, "Edge-preserving smoothers for image processing," *Journal of the American Statistical Association*, vol. 93, no. 442, pp. 526–541, 1998.
- [18] D. L. Donoho and I. M. Johnstone, "Minimax estimation via wavelet shrinkage," *The annals of Statistics*, vol. 26, no. 3, pp. 879–921, 1998.
- [19] G. Yu and G. Sapiro, "DCT Image Denoising: a Simple and Effective Image Denoising Algorithm," *Image Processing On Line*, vol. 1, pp. 292–296, 2011.
- [20] M. Lebrun, A. Buades, and J.-M. Morel, "A nonlocal bayesian image denoising algorithm," *SIAM Journal on Imaging Sciences*, vol. 6, no. 3, pp. 1665–1688, 2013.
- [21] S. W. Zamir, A. Arora, S. Khan, M. Hayat, F. S. Khan, and M.-H. Yang, "Restormer: Efficient transformer for high-resolution image restoration," in *Proceedings of the IEEE/CVF conference on computer vision and pattern recognition*, 2022, pp. 5728–5739.
- [22] C. Saharia, J. Ho, W. Chan, T. Salimans, D. J. Fleet, and M. Norouzi, "Image super-resolution via iterative refinement," *IEEE transactions on pattern analysis and machine intelligence*, vol. 45, no. 4, pp. 4713–4726, 2022.
- [23] Z. Kadhodaie and E. Simoncelli, "Stochastic solutions for linear inverse problems using the prior implicit in a denoiser," *Advances in Neural Information Processing Systems*, vol. 34, pp. 13 242–13 254, 2021.
- [24] P. Liu, H. Zhang, K. Zhang, L. Lin, and W. Zuo, "Multi-level wavelet-cn for image restoration," in *Proceedings of the IEEE conference on computer vision and pattern recognition workshops*, 2018, pp. 773–782.
- [25] C. Cruz, A. Foi, V. Katkovnik, and K. Egiazarian, "Nonlocality-reinforced convolutional neural networks for image denoising," *IEEE Signal Processing Letters*, vol. 25, no. 8, pp. 1216–1220, 2018.
- [26] D. Valsesia, G. Fracastoro, and E. Magli, "Deep graph-convolutional image denoising," *IEEE Transactions on Image Processing*, vol. 29, pp. 8226–8237, 2020.
- [27] J. Johnson, A. Alahi, and L. Fei-Fei, "Perceptual losses for real-time style transfer and super-resolution," in *Computer Vision—ECCV 2016: 14th European Conference, Amsterdam, The Netherlands, October 11–14, 2016, Proceedings, Part II 14*. Springer, 2016, pp. 694–711.
- [28] M. S. Sajjadi, B. Scholkopf, and M. Hirsch, "Enhancenet: Single image super-resolution through automated texture synthesis," in *Proceedings of the IEEE international conference on computer vision*, 2017, pp. 4491–4500.
- [29] A. Dosovitskiy, P. Fischer, E. Ilg, P. Hausser, C. Hazirbas, V. Golkov, P. Van Der Smagt, D. Cremers, and T. Brox, "FlowNet: Learning optical flow with convolutional networks," in *Proceedings of the IEEE international conference on computer vision*, 2015, pp. 2758–2766.
- [30] D. Sun, D. Vlastic, C. Herrmann, V. Jampani, M. Krainin, H. Chang, R. Zabih, W. T. Freeman, and C. Liu, "Autoflow: Learning a better training set for optical flow," in *Proceedings of the IEEE/CVF Conference on Computer Vision and Pattern Recognition*, 2021, pp. 10 093–10 102.
- [31] Y. Chen, W. Li, X. Chen, and L. V. Gool, "Learning semantic segmentation from synthetic data: A geometrically guided input-output adaptation approach," in *Proceedings of the IEEE/CVF conference on computer vision and pattern recognition*, 2019, pp. 1841–1850.
- [32] D. Ward, P. Moghadam, and N. Hudson, "Deep leaf segmentation using synthetic data," *arXiv preprint arXiv:1807.10931*, 2018.
- [33] S. Hinterstoisser, O. Pauly, H. Heibel, M. Martina, and M. Bokeloh, "An annotation saved is an annotation earned: Using fully synthetic training for object detection," in *Proceedings of the IEEE/CVF international conference on computer vision workshops*, 2019, pp. 0–0.
- [34] M. Frid-Adar, E. Klang, M. Amitai, J. Goldberger, and H. Greenspan, "Synthetic data augmentation using gan for improved liver lesion classification," in *2018 IEEE 15th international symposium on biomedical imaging (ISBI 2018)*. IEEE, 2018, pp. 289–293.
- [35] G. Ros, L. Sellart, J. Materzynska, D. Vazquez, and A. M. Lopez, "The synthia dataset: A large collection of synthetic images for semantic segmentation of urban scenes," in *Proceedings of the IEEE conference on computer vision and pattern recognition*, 2016, pp. 3234–3243.
- [36] C. Gan, J. Schwartz, S. Alter, D. Mrowca, M. Schrimpf, J. Traer, J. De Freitas, J. Kubilius, A. Bhandwalder, N. Haber *et al.*, "Threedworld: A platform for interactive multi-modal physical simulation," *arXiv preprint arXiv:2007.04954*, 2020.
- [37] K. Greff, F. Belletti, L. Beyer, C. Doersch, Y. Du, D. Duckworth, D. J. Fleet, D. Gnanaprasam, F. Golemo, C. Herrmann *et al.*, "Kubric: A scalable dataset generator," in *Proceedings of the IEEE/CVF conference on computer vision and pattern recognition*, 2022, pp. 3749–3761.
- [38] Y. Zheng, A. W. Harley, B. Shen, G. Wetzstein, and L. J. Guibas, "Pointodyssey: A large-scale synthetic dataset for long-term point tracking," in *Proceedings of the IEEE/CVF International Conference on Computer Vision*, 2023, pp. 19 855–19 865.
- [39] S. R. Richter, V. Vineet, S. Roth, and V. Koltun, "Playing for data: Ground truth from computer games," in *Computer Vision—ECCV 2016: 14th European Conference, Amsterdam, The Netherlands, October 11–14, 2016, Proceedings, Part II 14*. Springer, 2016, pp. 102–118.
- [40] Y. Zhang, H. Ling, J. Gao, K. Yin, J.-F. Lafleche, A. Barriuso, A. Torralba, and S. Fidler, "Datasetgan: Efficient labeled data factory with minimal human effort," in *Proceedings of the IEEE/CVF Conference on Computer Vision and Pattern Recognition*, 2021, pp. 10 145–10 155.
- [41] K. Shmelkov, C. Schmid, and K. Alahari, "How good is my gan?" in *Proceedings of the European conference on computer vision (ECCV)*, 2018, pp. 213–229.
- [42] M. B. Saryıldız, K. Alahari, D. Larlus, and Y. Kalantidis, "Fake it till you make it: Learning transferable representations from synthetic imagenet clones," in *Proceedings of the IEEE/CVF Conference on Computer Vision and Pattern Recognition*, 2023, pp. 8011–8021.
- [43] H. Kataoka, K. Okayasu, A. Matsumoto, E. Yamagata, R. Yamada, N. Inoue, A. Nakamura, and Y. Satoh, "Pre-training without natural images," in *Proceedings of the Asian Conference on Computer Vision*, 2020.
- [44] S. Takashima, R. Hayamizu, N. Inoue, H. Kataoka, and R. Yokota, "Visual atoms: Pre-training vision transformers with sinusoidal waves," in *Proceedings of the IEEE/CVF Conference on Computer Vision and Pattern Recognition*, 2023, pp. 18 579–18 588.
- [45] R. Shinoda, R. Hayamizu, K. Nakashima, N. Inoue, R. Yokota, and H. Kataoka, "Segrcdb: Semantic segmentation via formula-driven supervised learning," in *Proceedings of the IEEE/CVF International Conference on Computer Vision*, 2023, pp. 20 054–20 063.
- [46] C. Anderson and R. Farrell, "Improving fractal pre-training," in *Proceedings of the IEEE/CVF Winter Conference on Applications of Computer Vision*, 2022, pp. 1300–1309.
- [47] D. L. Ruderman, "Origins of scaling in natural images," *Vision research*, vol. 37, no. 23, pp. 3385–3398, 1997.
- [48] M. Baradad, J. Wulff, T. Wang, P. Isola, and A. Torralba, "Learning to see by looking at noise," *Advances in Neural Information Processing Systems*, vol. 34, 2021.
- [49] P. C. Madhusudana, S.-J. Lee, and H. R. Sheikh, "Revisiting dead leaves model: Training with synthetic data," *IEEE Signal Processing Letters*, 2021.
- [50] Y. Gousseau and F. Roueff, "Modeling occlusion and scaling in natural images," *Multiscale Modeling & Simulation*, vol. 6, no. 1, pp. 105–134, 2007.
- [51] T. Auer and M. Held, "Heuristics for the generation of random polygons," in *CCCG*, 1996, pp. 38–43.
- [52] A. P. Tomás and A. L. Bajuelos, "Generating random orthogonal polygons," in *Conference on Technology Transfer*. Springer, 2003, pp. 364–373.
- [53] H. Edelsbrunner, D. Kirkpatrick, and R. Seidel, "On the shape of a set of points in the plane," *IEEE Transactions on information theory*, vol. 29, no. 4, pp. 551–559, 1983.
- [54] GEOS contributors, *GEOS computational geometry library*, Open Source Geospatial Foundation, 2025. [Online]. Available: <https://libgeos.org/>
- [55] J. Portilla and E. P. Simoncelli, "A parametric texture model based on joint statistics of complex wavelet coefficients," *International journal of computer vision*, vol. 40, pp. 49–70, 2000.

- [56] L. Gatys, A. S. Ecker, and M. Bethge, "Texture synthesis using convolutional neural networks," *Advances in neural information processing systems*, vol. 28, 2015.
- [57] A. A. Efros and T. K. Leung, "Texture synthesis by non-parametric sampling," in *Proceedings of the seventh IEEE international conference on computer vision*, vol. 2. IEEE, 1999, pp. 1033–1038.
- [58] L.-Y. Wei and M. Levoy, "Fast texture synthesis using tree-structured vector quantization," in *Proceedings of the 27th annual conference on Computer graphics and interactive techniques*, 2000, pp. 479–488.
- [59] R. Achddou, Y. Gousseau, and S. Ladjal, "Learning raw image denoising using a parametric color image model," in *2023 IEEE International Conference on Image Processing (ICIP)*. IEEE, 2023, pp. 2690–2694.
- [60] E. Meinhardt-Llopis and M. Micheli, "Implementation of the centroid method for the correction of turbulence," *Image Processing On Line*, vol. 4, pp. 187–195, 2014.
- [61] B. Galerne, Y. Gousseau, and J.-M. Morel, "Random phase textures: Theory and synthesis," *IEEE Transactions on image processing*, vol. 20, no. 1, pp. 257–267, 2010.
- [62] D. L. Ruderman and W. Bialek, "Statistics of natural images: Scaling in the woods," *Physical review letters*, vol. 73, no. 6, p. 814, 1994.
- [63] G. J. Burton and I. R. Moorhead, "Color and spatial structure in natural scenes," *Applied optics*, vol. 26, no. 1, pp. 157–170, 1987.
- [64] J. Demers, "Depth of field: A survey of techniques," *Gpu Gems*, vol. 1, no. 375, p. U390, 2004.
- [65] C. Scofield, "212-d depth-of-field simulation for computer animation," in *Graphics Gems III (IBM Version)*. Elsevier, 1992, pp. 36–38.
- [66] J. Johnson, B. Hariharan, L. Van Der Maaten, L. Fei-Fei, C. Lawrence Zitnick, and R. Girshick, "Clevr: A diagnostic dataset for compositional language and elementary visual reasoning," in *Proceedings of the IEEE conference on computer vision and pattern recognition*, 2017, pp. 2901–2910.
- [67] K. Ma, Z. Duanmu, Q. Wu, Z. Wang, H. Yong, H. Li, and L. Zhang, "Waterloo Exploration Database: New challenges for image quality assessment models," *IEEE Transactions on Image Processing*, vol. 26, no. 2, pp. 1004–1016, Feb. 2017.
- [68] E. Agustsson and R. Timofte, "Ntire 2017 challenge on single image super-resolution: Dataset and study," in *The IEEE Conference on Computer Vision and Pattern Recognition (CVPR) Workshops*, July 2017.
- [69] B. Lim, S. Son, H. Kim, S. Nah, and K. Mu Lee, "Enhanced deep residual networks for single image super-resolution," in *Proceedings of the IEEE conference on computer vision and pattern recognition workshops*, 2017, pp. 136–144.
- [70] M. Tassano, J. Delon, and T. Veit, "An analysis and implementation of the ffdnet image denoising method," *Image Processing On Line*, vol. 9, pp. 1–25, 2019.
- [71] R. Franzen, "Kodak lossless true color image suite," source: <http://r0k.us/graphics/kodak>, vol. 4, no. 2, p. 9, 1999.
- [72] D. Martin, C. Fowlkes, D. Tal, and J. Malik, "A database of human segmented natural images and its application to evaluating segmentation algorithms and measuring ecological statistics," in *Proceedings eighth IEEE international conference on computer vision. ICCV 2001*, vol. 2. IEEE, 2001, pp. 416–423.
- [73] L. Zhang, X. Wu, A. Buades, and X. Li, "Color demosaicking by local directional interpolation and nonlocal adaptive thresholding," *Journal of Electronic imaging*, vol. 20, no. 2, pp. 023 016–023 016, 2011.
- [74] J.-B. Huang, A. Singh, and N. Ahuja, "Single image super-resolution from transformed self-exemplars," in *Proceedings of the IEEE conference on computer vision and pattern recognition*, 2015, pp. 5197–5206.
- [75] A. Ignatov, J. Patel, and R. Timofte, "Rendering natural camera bokeh effect with deep learning," in *Proceedings of the IEEE/CVF Conference on Computer Vision and Pattern Recognition Workshops*, 2020, pp. 418–419.
- [76] J. Liang, J. Cao, G. Sun, K. Zhang, L. Van Gool, and R. Timofte, "Swinir: Image restoration using swin transformer," in *Proceedings of the IEEE/CVF international conference on computer vision*, 2021, pp. 1833–1844.
- [77] R. Zeyde, M. Elad, and M. Protter, "On single image scale-up using sparse-representations," in *Curves and Surfaces: 7th International Conference, Avignon, France, June 24-30, 2010, Revised Selected Papers 7*. Springer, 2012, pp. 711–730.
- [78] A. Levin, Y. Weiss, F. Durand, and W. T. Freeman, "Understanding and evaluating blind deconvolution algorithms," in *2009 IEEE conference on computer vision and pattern recognition*. IEEE, 2009, pp. 1964–1971.
- [79] M. Hein, M. Andriushchenko, and J. Bitterwolf, "Why relu networks yield high-confidence predictions far away from the training data and how to mitigate the problem," in *Proceedings of the IEEE/CVF conference on computer vision and pattern recognition*, 2019, pp. 41–50.
- [80] T. Cohen and M. Welling, "Group equivariant convolutional networks," in *International conference on machine learning*. PMLR, 2016, pp. 2990–2999.

Supplementary Material: VibrantLeaves

S8. BACKGROUND ON THE DEAD LEAVES IMAGE MODEL

The dead leaves model is a random field obtained as the sequential superimposition of random shapes. It is defined (see [1], [2]) from a set of random positions, times and shapes $\{(x_i, t_i, X_i)_{i \in \mathbb{N}}$, where $\mathcal{P} = \sum \delta_{x_i, t_i}$ is a homogeneous Poisson process on $\mathbb{R}^2 \times (-\infty, 0]$ and the X_i are random sets of \mathbb{R}^2 that are independent of \mathcal{P} . The sets $x_i + X_i$ are called *leaves* and for each i , the *visible part* of the leaf is defined as

$$V_i = (x_i + X_i) \setminus \bigcup_{t_j \in (t_i, 0)} (x_j + X_j),$$

that is, the visible part of the leaf (x_i, t_i, X_i) is obtained by removing from this leaf all leaves that are indexed by a time greater than t_i (that falls after it). The dead leaves model is then defined as the collection of all visible parts. A random image can be obtained by assigning a random gray level (or color) to each visible part.

A particular type of dead leaves model, where the leaves have a size distribution with scaling properties, has been shown to reproduce important statistical properties of natural images [3], [4]. Such models are obtained by considering random leaves $R.X$, where X is a given shape and R is a real random variable with density $f(r) = C.r^{-\gamma}$, with C a normalizing constant. The case $\gamma = 3$ corresponds to a scale invariant model [4]. In order for such models to be well defined, values of R have to be restricted to values in (r_{\min}, r_{\max}) , see [5] for a detailed mathematical analysis. The resulting model therefore depends on 3 parameters: r_{\min} , r_{\max} and γ . This model is especially appealing for natural images, because it incorporates in a very simple setting two of their most fundamental property: non Gaussianity (as a result of edges) and scaling properties [6]. Because this model contains details and edges at all scales, potentially of arbitrary contrast, it has been proposed as a tool for the evaluation of the ability of imaging devices to faithfully capture textures [7] and was thereafter retained as a standard for image quality evaluation [8].

Dead leaves images were first employed for deep image restoration in [9], where the authors identify several critical factors contributing to the success of their method, including the size distribution, a downscaling operation as a basic image acquisition model, and a color sampling algorithm. For each generated dead leaves image, colors are sampled from the color histogram of a randomly selected image from a large set of natural images. We stress here that it is important to sample colors from a single natural image each time, and not from a global color model, which would result in a too strong homogeneity and little variety (see [9]). It was later shown that these histograms could be approximated using a sophisticated parametric model [10] without compromising performance. For simplicity, we sample colors directly from natural images for the remainder of this work.

S9. VIBRANTLEAVES IMPLEMENTATION DETAILS

A. VibrantLeaves function

The **VL** function first calls the histogram sampling function, which picks a random color image in the Waterloo database [11]. It then calls the **LeavesStack** function three times to generate a background, a middle-ground and a foreground stack. Each of these calls are generated with the same parameters except the coverage percentage p which we chose to be $p_b = 100\%$ for the background, $p_m = 50\%$ for the middleground and $p_f = 25\%$ for the foreground. These are then merged according to the depth-of-field method presented in Section III-C1. The standard deviations of each blur kernels are chosen equal ($\sigma_1 = \sigma_2$) and are sampled from a power law $p(\sigma_1) = C.\mathbb{1}_{[0,10]}(\sigma_1).\sigma_1^{0.5}$ of exponent 0.5 so that larger blur values appear more scarcely than average or small blur values. The image is then downscaled to ensure no aliasing artifacts caused by the artificially sharp edges of the synthesized shapes. This operation is performed with a bilinear downscaling of 2 and respects Shannon sampling conditions, by first blurring with an appropriate Gaussian kernel. The parameters of the function **VL** are summarized in Table S1.

Size	Coverage			DoF			Post-Proc.
w	p_b	p_m	p_f	σ_{\min}	σ_{\max}	α_{blur}	\downarrow
1024	100	50	25	0	10	0.5	2

TABLE S1: Parameters of VibrantLeaves

B. The LeavesStack function

This function performs the same operations iteratively until a portion p of the image plane is covered. *First*, the (x, y) positions of the shapes are sampled uniformly at random in the image plane.

Second, we generate a random shape with the `SampleShape` function of radius r sampled with a clipped power law density f which follows

$$f(r) \sim C.\mathbb{1}_{[r_{\min}, r_{\max}]}(r).r^{-\alpha},$$

where C is a normalizing constant. The radius parameters are the following: $r_{\min} = 10$ and $r_{\max} = 512$.

Third, we generate a texture map with the `SampleTexture` function. Finally, we multiply the shape mask with this texture map to obtain our colored shape, and update the corresponding pixels of the current image. The parameters of the function `LeavesStack` are summarized in Table S2.

r_{\min}	r_{\max}	α
10	512	3

TABLE S2: Parameters of LeavesStack

C. The SampleShape function

This function samples a random shape following the principles presented in Section III-A. To generate a random shape

of radius r , we sample n points uniformly in a disc D_r . For shape diversity, we sample the α -shape parameter uniformly in $[0.2, 0.6]$ (larger values lead to regular shapes that are close to the convex hull of the random points). Smoothing is applied to half the shapes, with a Gaussian kernel of standard deviation sampled uniformly in $[1, 10]$ (values over 10 often cause disconnected shapes, as a result of the rough approximation of the curvature motion employed). In addition to these shapes, we also sample disks and rectangles. The parameters of the function `SampleShape` are summarized in Table S3.

Nb of points n	Concavity α	Smoothing		Proportions		
		σ_s	p_{smooth}	p_{poly}	$p_{\text{rectangle}}$	p_{disks}
$\mathcal{U}([10, 100])$	$\mathcal{U}([0.2, 0.6])$	$\mathcal{U}([1, 10])$	1/2	2/3	1/6	1/6

TABLE S3: Parameters of `SampleShape`

D. The `SampleTexture` function

The proportion of pseudo-periodic texture is chosen to be 1/6, the one of micro-texture is 2/3 and the one of 2-scale texture is 1/6. The reason for this is that having too many sinusoidal textures in the data set leads to the reproduction of sinusoidal artifacts in the denoised images. For micro-textures, the slope of the power spectrum is sampled uniformly at random in $[0.5, 2.5]$ to get a similar amount of smooth and harsh micro-textures. For pseudo-periodic patterns and interpolation masks, we chose $T_{\text{min}} = 5$ and $T_{\text{max}} = 100$, to get short and long oscillations. The sharpening parameter of the logit function is sampled with: $\lambda \sim \mathcal{U}([1, 10])$. As mentioned in the manuscript, we also apply a thresholding operations to all pseudo-periodic textures, with a threshold $\tau_{\text{texture}} \sim \mathcal{U}([-1, 1])$. The atmospheric disturbance presented in Section III-B1 is applied to half of these textures, and so is the perspective transform presented in Section III-C2. The parameters of the function `SampleTexture` are summarized in Table S4.

Proportions			Periodic text.			Colored noise
$p_{\text{p.p.}}$	$p_{\text{c.n.}}$	$p_{\text{b.t.}}$	T	λ	τ_{texture}	γ
1/6	2/3	1/6	$\mathcal{U}([5, 100])$	$\mathcal{U}([1, 10])$	$\mathcal{U}([-1, 1])$	$\mathcal{U}([0, 5, 2.5])$

TABLE S4: Parameters of `SampleTexture`

S10. ABLATION STUDY RESULTS

In Fig. S1, we report some examples of the ablation study results from Section VI-B. These visual examples show the importance of the role of texture modeling, depth, and geometry.

S11. ADDITIONAL SAMPLE VISUALIZATIONS OF VIBRANTLEAVES IMAGES

REFERENCES

[1] G. Matheron, “Modele séquentiel de partition aléatoire,” Technical report, CMM, Tech. Rep., 1968.
 [2] C. Bordenave, Y. Gousseau, and F. Roueff, “The dead leaves model: a general tessellation modeling occlusion,” *Advances in applied probability*, vol. 38, no. 1, pp. 31–46, 2006.

[3] L. Alvarez, Y. Gousseau, and J.-M. Morel, “The size of objects in natural and artificial images,” in *Advances in Imaging and Electron Physics*. Elsevier, 1999, vol. 111, pp. 167–242.
 [4] A. B. Lee, D. Mumford, and J. Huang, “Occlusion models for natural images: A statistical study of a scale-invariant dead leaves model,” *International Journal of Computer Vision*, vol. 41, no. 1-2, pp. 35–59, 2001.
 [5] Y. Gousseau and F. Roueff, “Modeling occlusion and scaling in natural images,” *Multiscale Modeling & Simulation*, vol. 6, no. 1, pp. 105–134, 2007.
 [6] D. Mumford and B. Gidas, “Stochastic models for generic images,” *Quarterly of applied mathematics*, vol. 59, no. 1, pp. 85–111, 2001.
 [7] F. Cao, F. Guichard, and H. Hornung, “Dead leaves model for measuring texture quality on a digital camera,” in *Digital Photography VI*, vol. 7537. International Society for Optics and Photonics, 2010, p. 75370E.
 [8] “Photography – Digital cameras – Part 2: Texture analysis using stochastic pattern,” International Organization for Standardization, Geneva, CH, Standard, 2019.
 [9] R. Achddou, Y. Gousseau, and S. Ladjal, “Synthetic images as a regularity prior for image restoration neural networks,” in *International Conference on Scale Space and Variational Methods in Computer Vision*. Springer, 2021, pp. 333–345.
 [10] —, “Learning raw image denoising using a parametric color image model,” in *2023 IEEE International Conference on Image Processing (ICIP)*. IEEE, 2023, pp. 2690–2694.
 [11] K. Ma, Z. Duanmu, Q. Wu, Z. Wang, H. Yong, H. Li, and L. Zhang, “Waterloo Exploration Database: New challenges for image quality assessment models,” *IEEE Transactions on Image Processing*, vol. 26, no. 2, pp. 1004–1016, Feb. 2017.

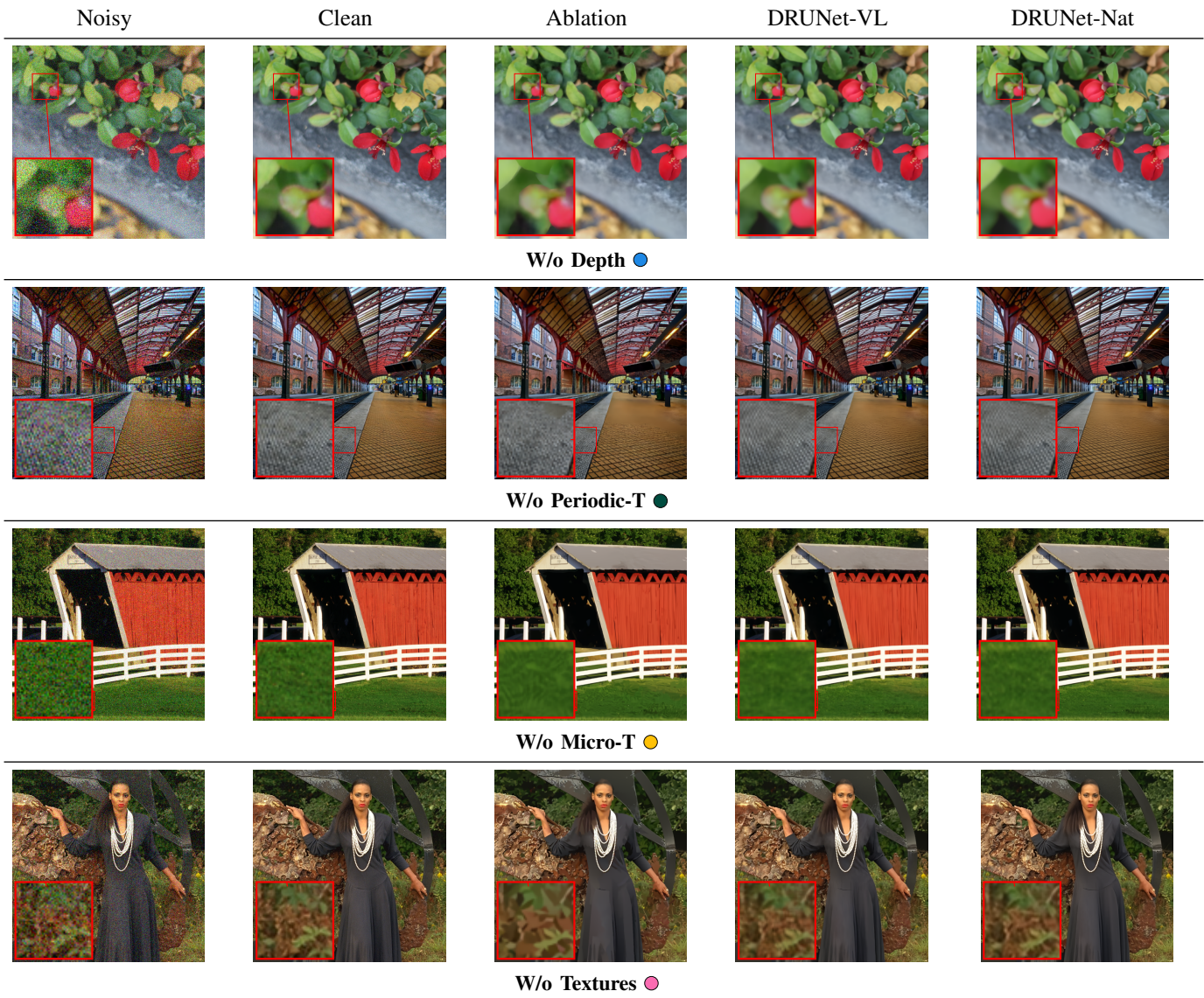


Fig. S1: Ablation Study - Visual Comparisons. We compare here the ablated models to the models trained on either VL or Natural Images. Each row correspond to a single ablated model. Visually our version of DRUNet trained on VL images surpasses the ablated models, and is visually close to DRUNet_{Nat}.



Fig. S2: Additional samples from the Vibrant Leaves model. The examples display diverse texture patterns, color profiles, object shape distributions, and depth-of field.